

When Gradient Optimization Is Not Enough: † Dispersive and Anchoring Geometric Regularizer for Multimodal Learning

Zixuan Xia ^{*1,2} Hao Wang ^{*1,2} Pengcheng Weng ^{*1,2} Yanyu Qian ^{3,2} Yangxin Xu ² William Dan ^{1,2} Fei Wang ²

Abstract

Multimodal learning aims to integrate complementary information from heterogeneous modalities, yet strong optimization alone does not guarantee well-structured representations. Even under carefully balanced training schemes, multimodal models often exhibit geometric pathologies, including intra-modal representation collapse and sample-level cross-modal inconsistency, which degrade both unimodal robustness and multimodal fusion.

We identify representation geometry as a missing control axis in multimodal learning and propose DAGR, a lightweight geometry-aware regularization framework. DAGR enforces two complementary constraints on intermediate embeddings: an intra-modal dispersive regularization that promotes representation diversity, and an inter-modal anchoring regularization that bounds sample-level cross-modal drift without rigid alignment. The proposed regularizer is plug-and-play, requires no architectural modifications, and is compatible with various training paradigms.

Extensive experiments across multiple multimodal benchmarks demonstrate consistent improvements in both multimodal and unimodal performance, showing that explicitly regulating representation geometry effectively mitigates modality trade-offs.

1. Introduction

Multimodal learning promises robustness by integrating complementary signals from different modalities (e.g., audio and vision) (Baltrušaitis et al., 2018). In practice, how-

¹Department of Informatics, University of Bern, Bern, Switzerland

²School of Software Engineering, Xi'an Jiaotong University, Xi'an, China

³College of Computing and Data Science, Nanyang Technological University, Singapore. Correspondence to: Fei Wang <feynmanw@xjtu.edu.cn>.

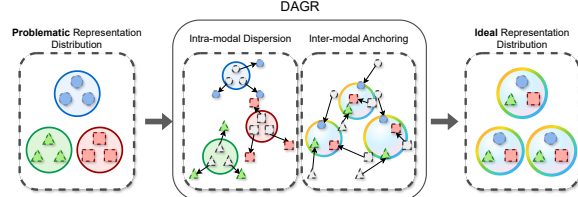


Figure 1. Progressive geometric alignment in multimodal representation learning. (Left) Modality-dominated geometry: embeddings are primarily organized by modality, leading to compact but isolated modality-specific clusters and poor cross-modal semantic alignment. (Middle) Regularized dispersion and anchoring: intra-modal dispersion encourages samples within each modality to spread out, while inter-modal anchoring pulls semantically corresponding samples across modalities closer, progressively reshaping the representation geometry. (Right) Semantically aligned geometry: embeddings corresponding to the same semantic concept across different modalities form coherent, modality-invariant clusters, yielding a well-aligned multimodal representation space.

ever, improved multimodal fusion accuracy often comes with an undesirable side effect: modality trade-offs (Wei & Hu, 2024), where enhancing one modality degrades another, yielding suboptimal unimodal performance under missing or corrupted modalities (Chaudhuri et al., 2025). While such trade-offs are frequently attributed to optimization issues (e.g., gradient suppression or objective conflicts) (Wei et al., 2025; Yu et al., 2020), we observe a recurring failure mode across multimodal training pipelines: modality encoders can exhibit **representation collapse** and **cross-modal inconsistency**, where each modality collapses into a narrow embedding subspace with reduced diversity and lower effective dimension, or different modalities become overly overlapping. We argue that such phenomena are not only optimization artifacts, but also reflect a more fundamental and largely overlooked factor: **geometric pathologies** of representation spaces, which not only limit the expressive capacity of modality-specific features but also reduce each modality's unique contribution to multimodal fusion. As illustrated in Fig. 1, these pathologies manifest as collapsed intra-modal structures and irregular sample-level misalignment across modalities.

To address these pathologies, we propose a **geometric regularizer** (DAGR), which adopts a **dispersive-and-anchoring**

mechanism along two complementary axes. **(i) Intra-modal dispersion** repels different samples within the same modality in a training mini-batch, maximizing representation diversity and preventing collapse within each modality encoder. This is inspired by dispersive representation regularization that spreads embeddings without requiring paired positives or heavy augmentations (Wang & He, 2025). **(ii) Inter-modal anchoring** preserves sample-level coherence by introducing a soft constraint that upper-bounds the geometric distance between modality-specific embeddings of the same sample without enforcing global encoder-level alignment. Notably, the proposed regularizer is agnostic to the underlying training paradigm (fusion-based, contrastive, or gradient-routed), allowing it to serve as a lightweight, plug-and-play add-on to intermediate embeddings of existing multimodal models without any architectural modifications.

We evaluate the proposed plug-and-play regularizer across diverse benchmarks, including CREMA-D, Kinetics-Sounds (KS), CUBICC and XRF55. Empirical results demonstrate that our method consistently boosts multimodal performance while simultaneously enhancing unimodal accuracy. By mitigating modality trade-offs, it proves that superior multimodal learning need not be achieved at the expense of modality-specific representations. Our contributions can be summarized as follows:

- We identify representation collapse and cross-modal inconsistency as geometric failure modes underlying modality trade-offs in multimodal learning.
- We propose DAGR, a lightweight, plug-and-play dispersion-anchoring geometric regularizer that promotes intra-modal diversity and inter-modal complementarity with no architectural changes.
- We provide extensive empirical and theoretical analysis showing improved multimodal fusion performance and consistently stronger unimodal representations.

2. Related Work

2.1. Gradient Optimization for Multimodal Learning

A central challenge in multimodal learning is the **modality trade-off**, where optimization dynamics tend to favor a “dominant” modality while suppressing others. Recent literature primarily addresses this via gradient-based balancing mechanisms that calibrate training signals at the logit or gradient level. For instance, online logit modulation has been proposed to harmonize modality-wise convergence rates (Zong et al., 2024), while gradient reweighting and projection strategies (e.g., those targeting “see-saw” dominance (Kwon et al., 2025)) explicitly counteract the competitive

nature of cross-modal updates. Furthermore, some studies reformulate multimodal training as a principled multi-objective optimization problem (Sener & Koltun, 2018; Yu et al., 2020), deriving algorithms that provide theoretical guarantees for mitigating gradient conflicts (Fernando et al., 2025; Jiang et al., 2025). Another line of research focuses on *decoupled* or *disentangled* optimization (Wang et al., 2024b; Wei et al., 2025). By separating the supervision pathways of unimodal encoders from the joint fusion module, these methods reduce inter-modal interference. A representative example is Disentangled Gradient Learning (DGL) (Wei et al., 2025), which detaches fusion-layer gradients and introduces independent unimodal supervision to ensure each encoder receives sufficient optimization signals. While these approaches significantly enhance training stability and unimodal strength by controlling where gradients flow and how weights are updated, they largely treat the resulting representation space as a black box.

2.2. Contrastive Alignment for Balancing Modalities

Another mainstream route tackles modality trade-offs using *contrastive learning* and *alignment-centric* objectives. By pulling matched cross-modal pairs together and pushing mismatched pairs apart, multimodal contrastive learning encourages shared semantics and can implicitly reduce the model’s over-reliance on a single modality, especially in retrieval and transfer settings (Radford et al., 2021; Alayrac et al., 2022; Wang & Isola, 2020). Recent analyses further reveal that multimodal contrastive objectives can induce systematic *modality gaps*—distributional separation between modalities in the shared space—linked to gradient-flow dynamics and objective conflicts (Yaras et al., 2024). In response, new objectives aim to better characterize or control what should be aligned. For instance, CoMM argues that naive cross-modal alignment tends to emphasize redundant/shared factors and proposes a communication-based contrastive formulation to capture richer multimodal interactions (Dufumier et al., 2024). Other concurrent studies revisit modality gaps and alignment limits under multimodal constraints (Yi et al., 2025).

2.3. Geometry-aware Regularization

Recent literature highlights embedding geometry, characterized by representational dispersion and minimized inconsistency, as a cornerstone of robust multimodal learning (Wang & Isola, 2020; Zbontar et al., 2021; Bardes et al., 2021). While efforts like UniAlign (Yin et al.) have explored the decoupling of alignment and uniformity, they primarily target shared-space tasks such as retrieval and generation. We contend that for the multimodal classification task, the modality imbalance problem is rooted as much in geometry as in optimization. Even under balanced gradient regimes, modality-specific representations can still succumb

to self-collapse or cross-modal inconsistency. Complementary to gradient-centric imbalance methods that modulate training dynamics (e.g., inconsistency-phase monitoring and gated gradient suppression in RedReg (Huang et al., 2025; Yang et al., 2025)), we introduce a plug-and-play geometry-aware regularizer designed to complement existing gradient-based strategies. Our approach operates on two disentangled geometric axes: (i) Intra-modal dispersion, which expands representation diversity to stave off unimodal collapse; and (ii) Constrained inter-modal consistency, which curbs cross-modal inconsistency without imposing the restrictive bottleneck of a globally shared embedding space. By shaping the encoders toward complementary geometric structures, it preserves each modality’s unique contribution while delegating the synthesis of shared evidence to the fusion module.

3. Methodology

3.1. Problem Setup and Geometric Motivation

Problem setup. Consider a supervised multimodal learning problem with a dataset $\mathcal{D} = \{(x_i, y_i)\}_{i=1}^N$, where each sample $x_i = (x_i^1, \dots, x_i^M)$ consists of M modalities and $y_i \in \{1, \dots, K\}$ denotes the label. Each modality is encoded by an encoder ϕ_m into a representation $z_i^m \in \mathbb{R}^d$. A standard multimodal training objective is

$$\mathcal{L} = \sum_{m=1}^M \mathcal{L}_{\text{CE}}(W_m z^m, y), \quad (1)$$

indicating that the representations of each modality can be individually supervised by the label to optimize the respective classifiers W_m .

To enhance multimodal learning, two empirical principles are widely recognized (Baltrušaitis et al., 2018): (i) **unimodal representation diversity**, where each modality maintains sufficient representation diversity to remain predictive on its own, and (ii) **cross-modal consistency**, where representations of the same sample across modalities remain coherently aligned without becoming redundant, which ensures that different modalities contribute complementary and non-substitutable cues for downstream tasks.

Despite strong empirical performance, we observe that the following failure modes can also emerge in practice, even when training pipelines are carefully designed:

Geometric Failure Modes

- **Intra-modal collapse:** Unimodal representations collapse into a narrow region of the embedding space, resulting in low-rank features.
- **Inter-modal inconsistency:** Paired cross-modal representations fail to remain reliably aligned, leading to redundant and weakly complementary

Algorithm 1 Training with DAGR

Require: Encoders $\{\phi_m\}_{m=1}^M$ (params $\{\theta_m\}$); step size η ;
 $\text{use_pareto}, \beta \in [0, 1]$ or $(\lambda_{\text{disp}}, \lambda_{\text{inter}})$

- 1: $\tilde{z}^{(m)} \leftarrow \text{Normalize}(\phi_m(x^{(m)}))$, $\forall m$
- 2: Compute $\mathcal{L}_{\text{disp}}^m$ and $\mathcal{L}_{\text{inter}}$
- 3: **for** $m = 1$ to M **do**
- 4: $g_{\text{task}}^{(m)} \leftarrow \nabla_{\theta_m} \mathcal{L}_{\text{task}}$
- 5: $g_{\text{disp}}^{(m)} \leftarrow \nabla_{\theta_m} \mathcal{L}_{\text{disp}}^m$; $g_{\text{inter}}^{(m)} \leftarrow \nabla_{\theta_m} \mathcal{L}_{\text{inter}}$
- 6: **if** use_pareto **then**
- 7: Solve α_m^* by Eq. (8)
- 8: $g_{\text{geom}}^{(m)} \leftarrow \beta(\alpha_m^* g_{\text{inter}}^{(m)} + (1 - \alpha_m^*) g_{\text{disp}}^{(m)})$
- 9: **else**
- 10: $g_{\text{geom}}^{(m)} \leftarrow \lambda_{\text{inter}} g_{\text{inter}}^{(m)} + \lambda_{\text{disp}} g_{\text{disp}}^{(m)}$
- 11: **end if**
- 12: $\theta_m \leftarrow \theta_m - \eta(g_{\text{task}}^{(m)} + g_{\text{geom}}^{(m)})$
- 13: **end for**

multimodal features.

We argue that such geometric failure modes stem from the inherent limitations of standard multimodal training objectives. Specifically, the objective admits a large family of formally optimal solutions; without additional fine-grained constraints, these solutions inevitably fall into geometric failure modes. (A formal proof is provided in Appendix A.1.)

To mitigate this, we propose DAGR, a dispersive and anchoring regularizer designed to enforce fine-grained geometric constraints upon multimodal representation learning, described next.

3.2. DAGR: Dispersive and Anchoring Geometry Regularization

To explicitly regulate multimodal representation geometry, we introduce DAGR (Dispersive and Anchoring Geometry Regularization) – a lightweight and plug-and-play geometric regularizer that complements existing multimodal training pipelines.

Technically, we first apply normalization to the unimodal representations to eliminate scale variations and project features onto a hypersphere. DAGR then enforces two synergistic geometric constraints: (i) a dispersive term that promotes the diversity and discriminability of intra-modal representations, and (ii) an anchoring term that maintains coherent cross-modal consistency. We next introduce the whole procedure in detail.

3.2.1. NORMALIZED UNIMODAL EMBEDDINGS

For each modality $m \in \{1, \dots, M\}$, let $z_i^m \in \mathbb{R}^d$ denote the encoder output for sample i . DAGR first projects z_i^m onto the unit hypersphere via ℓ_2 normalization: $\tilde{z}_i^m = \frac{z_i^m}{\|z_i^m\|_2}$.

This normalization removes scale ambiguity across samples, ensuring that subsequent regularization acts purely on the angular geometry of representations. Crucially, it also mitigates modality imbalance by aligning feature scales across modalities. Constraining representations to a shared unit hypersphere prevents dominant modalities from overwhelming optimization, thereby enabling balanced multimodal integration. In addition, the normalization is applied only within DAGR and does not restrict the expressiveness of the encoders.

3.2.2. INTRA-MODAL DISPERSIVE REGULARIZATION

To prevent unimodal representation collapse, DAGR first introduces an intra-modal dispersive regularization term that promotes sample-wise dispersion within each modality. Given a mini-batch \mathcal{B} of size B , we define a general class of dispersive objectives as

$$\mathcal{L}_{\text{disp}}^m = \frac{1}{B(B-1)} \sum_{\substack{i,j \in \mathcal{B} \\ i \neq j}} \psi(\|\tilde{z}_i^m - \tilde{z}_j^m\|_2), \quad (2)$$

where $\psi(\cdot)$ is a monotonically non-increasing potential function that assigns larger penalties to nearby pairs, thereby encouraging embeddings to spread out on the hypersphere. The overall intra-modal dispersive regularization term is obtained by averaging across modalities:

$$\mathcal{L}_{\text{intra}} = \frac{1}{M} \sum_{m=1}^M \mathcal{L}_{\text{disp}}^m. \quad (3)$$

The dispersive regularization in Eq. (2) can be instantiated using different monotonically non-increasing functions. In this work, we adopt a geometry-aware *uniformity-based radial basis function (RBF)* formulation. Given a set of ℓ_2 -normalized embeddings $\{\tilde{z}_i^m\}_{i=1}^N$ from modality m , the dispersive term is defined as

$$\mathcal{L}_{\text{disp}}^m = \log \mathbb{E}_{i \neq j} \left[\exp(-t \|\tilde{z}_i^m - \tilde{z}_j^m\|_2^2) \right], \quad (4)$$

where $t > 0$ controls the geometric scale of the interaction.

From a geometric perspective, Eq. (4) defines a soft energy over all pairwise distances, in which configurations with high local sample density are penalized more heavily. Pairs of embeddings that lie close to each other dominate the exponential term, thereby encouraging samples to disperse and occupy the unit hypersphere more uniformly. Compared to hard-margin or threshold-based repulsion, the RBF kernel induces smooth, isotropic forces that decay continuously with distance, yielding a well-behaved geometric prior.

This uniformity-driven regularization directly counteracts intra-modal representation collapse, where embeddings concentrate in a low-dimensional subspace or narrow region.

By promoting an approximately isotropic geometry with near-constant local density, the dispersive term preserves global structure within each modality and provides a stable geometric foundation upon which cross-modal anchoring can be more reliably enforced.

3.2.3. INTER-MODAL ANCHORING REGULARIZATION

While intra-modal dispersion effectively regularizes unimodal geometry, it does not explicitly constrain the relative geometric consistency across modalities, which may lead to cross-modal drift in the learned representation space. To mitigate this effect without enforcing full modality invariance, DAGR introduces a *bounded* inter-modal anchoring term that penalizes only *excessive* cross-modal discrepancy beyond a tolerance radius τ . Concretely, we define

$$\mathcal{L}_{\text{inter}} = \frac{1}{B} \sum_{i \in \mathcal{B}} \frac{1}{M(M-1)} \sum_{m \neq n} \left(\|\tilde{z}_i^m - \tilde{z}_i^n\|_2 - \tau \right)_+^2, \quad (5)$$

where $(x)_+ = \max(x, 0)$ and \tilde{z}_i^m denotes the ℓ_2 -normalized embedding on the unit hypersphere. Unlike naive alignment objectives that continuously shrink $\|\tilde{z}_i^m - \tilde{z}_i^n\|_2$, the proposed anchoring acts as a soft constraint that *upper-bounds* cross-modal drift up to the tolerance τ , while preserving modality-specific variations within this admissible radius. This bounded-drift behavior is theoretically characterized in Theorem 3.3.

3.2.4. OVERALL DAGR OBJECTIVE.

The final DAGR regularizer is defined as

$$\mathcal{L}_{\text{DAGR}} = \lambda_{\text{intra}} \mathcal{L}_{\text{intra}} + \lambda_{\text{inter}} \mathcal{L}_{\text{inter}}, \quad (6)$$

and is added to the underlying task objective: $\mathcal{L}_{\text{total}} = \mathcal{L} + \mathcal{L}_{\text{DAGR}}$. Algorithm 1 provides an overview of DAGR as a geometry-aware plugin integrated into a generic multimodal learning pipeline. DAGR operates directly on intermediate modality embeddings by applying dispersive and anchoring regularizations in parallel, thereby shaping the representation geometry without requiring any architectural modifications to the encoders or the fusion module.

3.2.5. ADAPTIVE PARETO-BALANCED WEIGHTING.

Although Eq. (6) defines DAGR as a weighted sum of $\mathcal{L}_{\text{intra}}$ and $\mathcal{L}_{\text{inter}}$, in practice the two terms may induce conflicting gradients on encoder parameters, leading to sensitivity to the choice of $(\lambda_{\text{intra}}, \lambda_{\text{inter}})$. To reduce manual tuning, we optionally adopt a Pareto-balanced weighting scheme that dynamically selects the mixing coefficient at each iteration.

Let θ_e denote the encoder parameters, and define

$$g_{\text{intra}} = \nabla_{\theta_e} \mathcal{L}_{\text{intra}}, \quad g_{\text{inter}} = \nabla_{\theta_e} \mathcal{L}_{\text{inter}}. \quad (7)$$

We seek a convex combination $g(\alpha) = \alpha g_{\text{inter}} + (1 - \alpha)g_{\text{intra}}$ that yields a stable descent direction by minimizing its norm:

$$\alpha^* = \arg \min_{\alpha \in [0,1]} \|\alpha g_{\text{inter}} + (1 - \alpha)g_{\text{intra}}\|_2^2. \quad (8)$$

This admits a closed-form solution

$$\alpha^* = \text{clip}_{[0,1]} \left(\frac{\|g_{\text{intra}}\|_2^2 - \langle g_{\text{inter}}, g_{\text{intra}} \rangle}{\|g_{\text{inter}} - g_{\text{intra}}\|_2^2} \right). \quad (9)$$

We then apply a geometry-gradient injection

$$g_{\text{geom}} = \beta(\alpha^* g_{\text{inter}} + (1 - \alpha^*)g_{\text{intra}}), \quad (10)$$

where β is a base scaling factor. Equivalently, this corresponds to using iteration-dependent weights $\lambda_{\text{inter}}^{(t)} = \beta\alpha^*$ and $\lambda_{\text{intra}}^{(t)} = \beta(1 - \alpha^*)$ in Eq. (6). Importantly, we apply Pareto balancing only to encoder parameters θ_e , while keeping the fusion module optimized solely by the task objective, thereby preserving DAGR as a plug-in geometry regularizer without architectural changes.

3.3. Theoretical Guarantees of DAGR

In the remainder of this section, we provide a theoretical analysis to demonstrate how DAGR resolves these geometric failure modes through the synergy of its two complementary regularizers. Specifically, we first prove that the intra-modal dispersive term $\mathcal{L}_{\text{intra}}$ induces repulsive forces that effectively preclude unimodal representation collapse. Subsequently, we establish that the inter-modal anchoring term $\mathcal{L}_{\text{inter}}$ rigorously bounds cross-modal drift, ensuring coherent alignment while safeguarding essential modality-specific variations.

3.3.1. DISPERSION VIA REPULSIVE GRADIENTS

We first show that a broad class of dispersive losses induces repulsive gradients on the unit hypersphere, leading to sample-wise repulsion that counteracts intra-modal collapse. And to be more specific, we then establish that, for the uniformity (RBF) instantiation, minimizing the dispersive loss is asymptotically equivalent to maximizing the Rényi-2 entropy of the representation distribution. This equivalence provides a strictly positive lower bound on the effective rank of the feature covariance matrix, theoretically ensuring representation diversity.

Lemma 3.1 (Repulsive gradients of dispersive potentials). *Let $\{\tilde{z}_i\}_{i=1}^B \subset \mathbb{S}^{d-1}$ denote a set of B embeddings constrained to a $(d-1)$ -dimensional unit hypersphere via ℓ_2 -normalization, and define the dispersive loss by Eq. (2), where $\psi : \mathbb{R}_{\geq 0} \rightarrow \mathbb{R}$ is non-increasing. Then for each i , any (sub)gradient admits*

$$\nabla_{\tilde{z}_i} \mathcal{L}_{\text{disp}}^m = \frac{2}{B(B-1)} \sum_{j \neq i} \psi'(\|\tilde{z}_i^m - \tilde{z}_j^m\|_2) (\tilde{z}_i^m - \tilde{z}_j^m), \quad (11)$$

where ψ' is the derivative when it exists (or any valid subderivative otherwise). Equivalently, the descent direction $-\nabla_{\tilde{z}_i} \mathcal{L}_{\text{disp}}^m$ is a nonnegative weighted sum of $(\tilde{z}_i^m - \tilde{z}_j^m)$.

Lemma 3.1 shows that a broad family of dispersive losses induces sample-wise repulsion on the hypersphere, directly addressing intra-modal collapse. This unifies common instantiations such as uniformity (RBF) and margin-based hinge repulsion.

While Lemma 3.1 provides a general geometric explanation, the RBF uniformity loss allows a stronger theoretical guarantee for avoiding representation collapse and low effective rank, stated in the following Theorem 3.2 and further verified experimentally in Section 4.3:

Theorem 3.2. *Minimizing the dispersive loss*

$$\mathcal{L}_{\text{disp}}^m = \log \mathbb{E}_{i \neq j} \left[\exp(-t\|\tilde{z}_i^m - \tilde{z}_j^m\|_2^2) \right] \quad (12)$$

is asymptotically equivalent to maximizing the Rényi-2 entropy $H_2(Z)$ of the feature distribution on the unit hypersphere. Consequently, for a sufficiently large weight λ_{intra} , the effective rank of the covariance $\Sigma_Z = \mathbb{E}[zz^\top]$ satisfies

$$\text{Rank}_{\text{eff}}(\Sigma_Z) \geq \gamma > 1,$$

where γ depends on the temperature t and batch statistics. A formal proof is provided in Appendix A.3.

3.3.2. ANCHORING BOUNDS CROSS-MODAL DRIFT.

Dispersion alone does not resolve the inter-modal inconsistency mode; DAGR addresses this via the anchoring term $\mathcal{L}_{\text{inter}}$, which couples representations across modalities at the sample level.

Theorem 3.3. *Consider the joint objective*

$$\mathcal{L}_{\text{total}} = \mathcal{L} + \lambda_{\text{inter}} \mathcal{L}_{\text{inter}} + \lambda_{\text{intra}} \mathcal{L}_{\text{intra}}, \quad (13)$$

where $\mathcal{L}_{\text{inter}} = \mathbb{E}[(\|\tilde{z}^m - \tilde{z}^n\|_2 - \tau)_+^2]$. Let \tilde{z}_*^m and \tilde{z}_*^n denote optimal representations of two modalities. Then the expected excess cross-modal drift satisfies

$$\mathbb{E}[(\|\tilde{z}_*^m - \tilde{z}_*^n\|_2 - \tau)_+^2] \leq \frac{\delta}{\lambda_{\text{inter}}}, \quad (14)$$

where $\delta \geq 0$ captures an irreducible modality gap induced by modality-specific nuisance factors. A formal proof is provided in Appendix A.4.

Remark 3.4. Unlike naive alignment objectives that enforce complete modality invariance, our anchoring formulation does not force $\|\tilde{z}_*^m - \tilde{z}_*^n\| \rightarrow 0$; instead, it suppresses cross-modal drift while allowing modality-specific deviations, which is crucial for preserving complementarity.

3.3.3. MAXIMUM-ENTROPY VIEW OF DAGR

Our regularizer also admits a maximum-entropy interpretation. After ℓ_2 normalization, each modality m induces a distribution over embeddings on the unit hypersphere. The intra-modal *dispersive* term promotes high-entropy (high effective-rank) unimodal representations, mitigating low-rank collapse and improving representation diversity (Thm. 3.2). Meanwhile, the inter-modal *anchoring* term imposes a *moment constraint* on cross-modal drift: it penalizes only the *excess* discrepancy beyond a tolerance radius τ , thereby suppressing semantic drift while preserving modality-specific variations.

Concretely, DAGR can be viewed as approximately solving the following moment-constrained maximum-entropy problem:

$$\max_{\theta} \sum_{m=1}^M H_2(Z_{\theta}^m) \quad \text{s.t.} \quad \mathbb{E} \left[(\|z^m - z^n\|_2 - \tau)_+^2 \right] \leq \epsilon, \quad (15)$$

where $H_2(\cdot)$ denotes the Rényi-2 entropy of the induced embedding distribution on the hypersphere, and ϵ specifies a drift budget. In words, DAGR seeks maximally diverse unimodal representations (high entropy / high effective rank) subject to a bounded cross-modal drift budget, rather than enforcing full modality invariance. See Appendix A.5 for additional discussion.

4. Experiments

4.1. Datasets and Experimental Setup

We evaluate the proposed method on a diverse set of multimodal benchmarks spanning audio–visual, tri-modal, image–text, and RF-based perception scenarios, including **CREMA-D** (Cao et al., 2014), **Kinetics-Sounds (KS)** (Arandjelovic & Zisserman, 2017), **CUB Image-Captions for Clustering (CUBICC)** (Palumbo et al., 2024) and **XRF55** (Wang et al., 2024a).

For audio–visual benchmarks (CREMA-D and KS), we follow the standardized experimental protocols and data splits provided by DGL (Wei et al., 2025). For image–text clustering on CUBICC, we adopt the official implementation of DCMEM (Gao et al., 2025). Experiments on XRF55 are conducted under the X-Fi framework (Chen & Yang, 2024), which provides unified preprocessing and evaluation for heterogeneous RF and vision modalities.

More details about datasets and the training setup are provided in Appendix B.1.

4.2. Main Results on Different Benchmarks

Results on CREMA-D and Kinetics-Sounds. Table 1 summarizes the results on the audio–visual benchmarks

CREMA-D and Kinetics-Sounds (KS). All methods are built upon the same DGL backbone, and **DGL + DAGR** corresponds to augmenting DGL with the proposed geometry-aware regularization.

Notably, **DGL + DAGR** improves not only multimodal accuracy but also unimodal performance for both audio and visual modalities. This behavior contrasts with many multimodal methods that improve fusion accuracy at the expense of unimodal representations, and suggests that explicitly regularizing representation geometry helps preserve modality-specific discriminability while enhancing cross-modal complementarity. Such results demonstrate that geometry-aware regularization effectively mitigates modality trade-offs in audio–visual learning.

Results on CUBICC. We further evaluate the proposed geometry-aware regularization on the CUB Image-Captions for Clustering (CUBICC) benchmark. Table 2 reports clustering results in terms of ACC, NMI, and ARI for image-only, caption-only, and joint representations. Compared to the original DCMEM baseline, augmenting the model with DAGR consistently improves clustering performance across all settings. In particular, for joint representations, our method achieves improvements of +3.5 ACC, +1.3 NMI, and +2.4 ARI, indicating more effective multimodal clustering. Notably, consistent gains are also observed for unimodal representations.

Since clustering performance is highly sensitive to the geometric structure of the embedding space, these results suggest that DAGR effectively reshapes representation geometry by enhancing inter-cluster separability while preserving intra-cluster compactness. Moreover, the consistent improvements on both unimodal and joint representations indicate that DAGR strengthens modality-specific structure without compromising cross-modal alignment, leading to more semantically coherent multimodal embeddings.

Results on XRF55 (X-Fi Benchmark). We further evaluate the proposed method on the XRF55 dataset under the X-Fi benchmark protocol. As shown in Table 3, incorporating DAGR consistently improves recognition accuracy across all modality settings, including unimodal and multimodal combinations.

Results Summary

Overall, across datasets of varying scales and modality compositions, DAGR consistently improves multimodal learning performance without sacrificing unimodal robustness, highlighting its ability to balance cross-modal integration and modality-specific representation quality across a wide range of experimental settings.

Table 1. Main results on CREMA-D and Kinetics-Sounds (KS). We report unimodal and multimodal classification accuracy.

Method	CREMA-D			KS		
	Audio	Visual	Multi	Audio	Visual	Multi
G-Blending (Wang et al., 2020)	58.78	58.62	69.21	46.35	51.12	69.60
OGM-GE (Peng et al., 2022)	57.76	40.09	68.82	44.23	45.81	66.89
PMR (Fan et al., 2023)	55.11	38.34	67.44	43.61	46.67	65.70
AGM (Li et al., 2023)	56.37	43.54	69.61	46.12	47.65	68.88
MMPareto (Wei & Hu, 2024)	59.43	61.09	70.12	48.40	52.42	69.83
D&R (Wei et al., 2024)	61.11	64.57	74.32	49.78	54.88	69.10
DGL (Wei et al., 2025)	62.17 \pm 0.79	70.31 \pm 1.11	77.65 \pm 1.05	50.63 \pm 0.54	59.83 \pm 0.63	75.44 \pm 0.49
DGL + DAGR (Ours)	62.98 \pm 0.50	72.10 \pm 0.55	78.16 \pm 0.38	50.83 \pm 0.50	61.71 \pm 0.47	77.00 \pm 0.44

Table 2. Clustering results on the CUB Image-Captions for Clustering (CUBICC) dataset. We report ACC, NMI, and ARI (%) for image-only, caption-only, and joint representations, and DCMEM +DAGR denotes augmenting DCMEM with the proposed geometry-aware dispersive regularization.

Method	Image			Caption			Joint		
	ACC	NMI	ARI	ACC	NMI	ARI	ACC	NMI	ARI
MVAE (Wu & Goodman, 2018)	26.2	12.4	7.5	18.1	2.4	0.9	38.7	26.8	18.0
MMVAE (Shi et al., 2019)	23.1	12.1	6.1	14.5	1.3	0.1	15.8	1.5	0.2
MoPoE (Sutter et al., 2021)	33.4	17.6	11.5	43.5	27.1	19.9	40.8	30.4	20.2
MEME (Joy et al., 2021)	44.8	43.4	28.4	36.3	29.5	18.6	19.8	4.8	2.1
MMVAE+ (Palumbo et al., 2023)	27.7	11.9	7.1	48.7	36.4	26.8	64.4	52.6	44.1
CMVAE (Palumbo et al., 2024)	67.7	58.3	47.4	65.1	53.3	42.7	73.7	67.4	57.2
MMVM (Sutter et al., 2024)	58.9	56.9	44.5	23.9	9.4	5.4	66.8	67.0	55.5
MVP (Gao & Pu, 2025)	64.1	53.8	41.8	48.5	34.4	26.1	61.1	55.6	44.0
DCMEM (Gao et al., 2025)	87.5	79.3	73.6	72.2	56.0	48.1	86.7	78.4	72.2
DCMEM +DAGR (Ours)	89.3	79.8	76.8	74.0	56.5	48.6	90.2	79.7	74.6

Table 3. Accuracy (%) on the XRF55 dataset under the X-Fi benchmark protocol. **X-Fi** denotes the benchmarked strong baseline in (Chen & Yang, 2024), and **X-Fi + DAGR** augments the corresponding pipeline with the proposed geometry-aware regularization. **Imp \uparrow** reports the absolute improvement over **X-Fi**.

Modality	X-Fi	X-Fi + DAGR	Imp \uparrow
R	82.33 \pm 1.23	83.57 \pm 0.04	+1.24
W	64.62 \pm 2.33	67.36 \pm 1.17	+2.74
RF	41.60 \pm 2.04	42.54 \pm 0.55	+0.94
R+W	89.92 \pm 0.74	90.74 \pm 0.18	+0.82
R+RF	83.76 \pm 1.70	85.84 \pm 0.15	+2.08
W+RF	67.49 \pm 0.36	67.95 \pm 0.38	+0.46
R+W+RF	90.09 \pm 0.82	91.01 \pm 0.06	+0.92

4.3. Ablation Studies

Component-wise ablation (dispersion vs. anchoring). We conduct a component-wise ablation study to disentangle the roles of the two geometric objectives in DAGR: intra-modal dispersion and inter-modal anchoring. Specifically, we evaluate four variants: ① the baseline training pipeline

without geometry regularization; ② applying only intra-modal dispersion $\mathcal{L}_{\text{intra}}$; ③ applying only inter-modal anchoring $\mathcal{L}_{\text{inter}}$; and ④ the full DAGR objective combining both components.

This ablation study provides a quantitative analysis of the complementary roles played by dispersion and anchoring, as summarized in Table 4. When applied individually, each component yields partial improvements. In particular, dispersion alone (②) leads to consistent gains in unimodal accuracy and also improves multimodal performance, suggesting its effectiveness in enhancing intra-modal geometry. Similarly, anchoring alone (③) benefits both unimodal and multimodal settings, with a more pronounced improvement in the multimodal score, indicating its role in stabilizing cross-modal relationships.

Importantly, neither component in isolation achieves uniformly optimal performance across all settings. When dispersion and anchoring are combined (④), the model attains the best overall balance, simultaneously strengthening unimodal robustness and multimodal fusion. This result highlights the complementary nature of the two ob-

Table 4. Component-wise ablation of geometry-aware regularization on CREMA-D. We report unimodal (Audio, Visual) and multimodal (Multi) classification accuracy.

Component		CREMA-D		
Disp	Anchor	Audio	Visual	Multi
✓		62.17±0.79	70.31±0.79	77.65±0.79
	✓	63.26±0.59	71.76±1.00	77.81±1.52
✓	✓	62.55±0.73	72.92±0.78	77.98±1.11
✓	✓	62.98±0.50	72.10±0.55	78.16±0.38

jectives and underscores the importance of jointly enforcing well-conditioned intra-modal geometry and consistent cross-modal alignment.

Hyper-parameter sensitivity. We further analyze the robustness of DAGR to hyper-parameter choices under two practical usage settings. In the direct regularization formulation, DAGR involves three hyper-parameters, namely λ_{intra} , λ_{inter} , and the temperature τ , which control intra-modal dispersion, inter-modal anchoring, and similarity sharpness, respectively. We sweep these parameters over a wide range on multiple datasets and observe smooth performance trends with well-defined optima, indicating that the method does not rely on fragile tuning.

To improve usability, we additionally adopt a Pareto-based formulation that automatically balances the two geometric objectives. Under this setting, only τ and a single trade-off coefficient β need to be tuned, substantially reducing the hyper-parameter search space. Empirically, we find that the Pareto formulation achieves comparable or better performance while exhibiting similar stability in both task metrics (unimodal and multimodal accuracy) and geometry diagnostics (e.g., effective rank and cross-modal drift).

Based on these observations, we use the Pareto-based variant as the default setting in our experiments. See Appendix D.1 for more details.

Robustness to Missing or Corrupted Modalities. In addition to standard ablations, we include a lightweight robustness evaluation to directly assess model behavior under missing or corrupted modalities. Specifically, at test time we progressively drop or corrupt one modality (e.g., random masking or noise injection) and report the degradation curves for both unimodal and multimodal performance, providing a more direct diagnosis of robustness than unimodal accuracy alone, and complements the component-wise ablation by revealing how DAGR affect stability under modality degradation. See Appendix D.2 for more details.

Additional baselines compared with Contrastive Learning. To rule out the possibility that our gains stem from

stronger cross-modal coupling or representation normalization, we evaluate several additional baselines on CREMA-D that are closely related to contrastive or invariance-driven objectives. Results are summarized in Appendix D.3.

Specifically, *Naive Align* enforces always-on per-sample cross-modal alignment. We further include VICReg-style and Barlow Twins-style objectives, which encourage invariance and redundancy reduction without relying on negative samples. Finally, the *Unit-sphere only* baseline isolates the effect of ℓ_2 normalization without introducing additional regularization terms.

Overall, none of these variants consistently match the performance of our method, indicating that the observed improvements cannot be attributed solely to contrastive alignment, feature normalization, or generic invariance constraints.

5. Conclusions, Limitations and Future Work

This work demonstrates that gradient-level optimization alone is insufficient for robust multimodal learning, as representation geometry can remain ill-conditioned even under carefully designed training schemes and carefully tuned objectives. By introducing DAGR, which explicitly promotes intra-modal dispersion and inter-modal anchoring at the geometric level, we consistently improve multimodal performance across audio-visual and heterogeneous multimodal benchmarks. Importantly, these gains are achieved without any other architectural modifications. The proposed method is therefore **plug-and-play**, lightweight, and can be seamlessly integrated into existing state-of-the-art multimodal training pipelines with minimal implementation overhead.

However, our evaluation focuses on medium-scale classification tasks and controlled backbone architectures. Extending this analysis to larger-scale datasets, more diverse task settings (e.g., temporal reasoning, generation, or cross-modal retrieval), and broader model families would further strengthen the empirical understanding of geometry-aware regularization. In particular, studying how geometric constraints interact with large transformer-based multimodal models, attention mechanisms, and temporal structure remains an open and promising direction. More broadly, we believe that similar geometric principles may also benefit self-supervised and weakly supervised multimodal learning, where representation collapse and misalignment are especially pronounced.

Impact Statement

This paper presents work whose goal is to advance the field of multimodal machine learning. There are many potential societal consequences of our work, none of which we feel must be specifically highlighted here.

References

Alayrac, J.-B., Donahue, J., Luc, P., Miech, A., Barr, I., Hasson, Y., Lenc, K., Mensch, A., Millican, K., Reynolds, M., et al. Flamingo: a visual language model for few-shot learning. *Advances in neural information processing systems*, 35:23716–23736, 2022.

Arandjelovic, R. and Zisserman, A. Look, listen and learn. In *Proceedings of the IEEE international conference on computer vision*, pp. 609–617, 2017.

Baltrušaitis, T., Ahuja, C., and Morency, L.-P. Multimodal machine learning: A survey and taxonomy. *IEEE transactions on pattern analysis and machine intelligence*, 41(2):423–443, 2018.

Bardes, A., Ponce, J., and LeCun, Y. Vicreg: Variance-invariance-covariance regularization for self-supervised learning. *arXiv preprint arXiv:2105.04906*, 2021.

Cao, H., Cooper, D. G., Keutmann, M. K., Gur, R. C., Nenkova, A., and Verma, R. Crema-d: Crowd-sourced emotional multimodal actors dataset. *IEEE transactions on affective computing*, 5(4):377–390, 2014.

Chaudhuri, A., Dutta, A., Bui, T., and Georgescu, S. A closer look at multimodal representation collapse. *arXiv preprint arXiv:2505.22483*, 2025.

Chen, X. and Yang, J. X-fi: A modality-invariant foundation model for multimodal human sensing. *arXiv preprint arXiv:2410.10167*, 2024.

Dufumier, B., Castillo-Navarro, J., Tuia, D., and Thiran, J.-P. What to align in multimodal contrastive learning? *arXiv preprint arXiv:2409.07402*, 2024.

Fan, Y., Xu, W., Wang, H., Wang, J., and Guo, S. Pmr: Prototypical modal rebalance for multimodal learning. In *Proceedings of the IEEE/CVF Conference on Computer Vision and Pattern Recognition*, pp. 20029–20038, 2023.

Fernando, H., Ram, P., Zhou, Y., Dan, S., Samulowitz, H., Baracaldo, N., and Chen, T. Mitigating modality imbalance in multi-modal learning via multi-objective optimization. *arXiv preprint arXiv:2511.06686*, 2025.

Gao, L., Chen, W., Wang, D., Guo, F., and Liang, C. Disentangled cross-modal representation learning with enhanced mutual supervision. In *The Thirty-ninth Annual Conference on Neural Information Processing Systems*, 2025.

Gao, X. and Pu, J. Deep incomplete multi-view learning via cyclic permutation of vaes. *arXiv preprint arXiv:2502.11037*, 2025.

Huang, C., Wei, Y., Yang, Z., and Hu, D. Adaptive unimodal regulation for balanced multimodal information acquisition. In *Proceedings of the Computer Vision and Pattern Recognition Conference*, pp. 25854–25863, 2025.

Jiang, Q.-Y., Chi, Z., and Yang, Y. Interactive multimodal learning via flat gradient modification. In *Proceedings of the Thirty-Fourth International Joint Conference on Artificial Intelligence*, pp. 5489–5497, 2025.

Joy, T., Shi, Y., Torr, P. H., Rainforth, T., Schmon, S. M., and Siddharth, N. Learning multimodal vaes through mutual supervision. *arXiv preprint arXiv:2106.12570*, 2021.

Kwon, J., Kim, M., Lee, E., Choi, J., and Kim, Y. Seesaw modality balance: See gradient, and sew impaired vision-language balance to mitigate dominant modality bias. *arXiv preprint arXiv:2503.13834*, 2025.

Li, H., Li, X., Hu, P., Lei, Y., Li, C., and Zhou, Y. Boosting multi-modal model performance with adaptive gradient modulation. In *Proceedings of the IEEE/CVF International Conference on Computer Vision*, pp. 22214–22224, 2023.

Palumbo, E., Daunhauer, I., and Vogt, J. E. Mmvae+: Enhancing the generative quality of multimodal vaes without compromises. In *The Eleventh International Conference on Learning Representations*. OpenReview, 2023.

Palumbo, E., Manduchi, L., Laguna, S., Chopard, D., and Vogt, J. E. Deep generative clustering with multimodal diffusion variational autoencoders. In *The Twelfth International Conference on Learning Representations*, 2024.

Peng, X., Wei, Y., Deng, A., Wang, D., and Hu, D. Balanced multimodal learning via on-the-fly gradient modulation. In *Proceedings of the IEEE/CVF conference on computer vision and pattern recognition*, pp. 8238–8247, 2022.

Radford, A., Kim, J. W., Hallacy, C., Ramesh, A., Goh, G., Agarwal, S., Sastry, G., Askell, A., Mishkin, P., Clark, J., et al. Learning transferable visual models from natural language supervision. In *International conference on machine learning*, pp. 8748–8763. PMLR, 2021.

Sener, O. and Koltun, V. Multi-task learning as multi-objective optimization. *Advances in neural information processing systems*, 31, 2018.

Shi, Y., Paige, B., Torr, P., et al. Variational mixture-of-experts autoencoders for multi-modal deep generative models. *Advances in neural information processing systems*, 32, 2019.

Sutter, T., Meng, Y., Agostini, A., Chopard, D., Fortin, N., Vogt, J., Shahbaba, B., and Mandt, S. Unity by diversity:

Improved representation learning for multimodal vaes. *Advances in Neural Information Processing Systems*, 37: 74262–74297, 2024.

Sutter, T. M., Daunhawer, I., and Vogt, J. E. Generalized multimodal elbo. *arXiv preprint arXiv:2105.02470*, 2021.

Wang, F., Lv, Y., Zhu, M., Ding, H., and Han, J. Xrf55: A radio frequency dataset for human indoor action analysis. *Proceedings of the ACM on Interactive, Mobile, Wearable and Ubiquitous Technologies*, 8(1):1–34, 2024a.

Wang, H., Luo, S., Hu, G., and Zhang, J. Gradient-guided modality decoupling for missing-modality robustness. In *Proceedings of the AAAI Conference on Artificial Intelligence*, volume 38, pp. 15483–15491, 2024b.

Wang, R. and He, K. Diffuse and disperse: Image generation with representation regularization. *arXiv preprint arXiv:2506.09027*, 2025.

Wang, T. and Isola, P. Understanding contrastive representation learning through alignment and uniformity on the hypersphere. In *International conference on machine learning*, pp. 9929–9939. PMLR, 2020.

Wang, W., Tran, D., and Feiszli, M. What makes training multi-modal classification networks hard? In *Proceedings of the IEEE/CVF conference on computer vision and pattern recognition*, pp. 12695–12705, 2020.

Wei, S., Luo, C., and Luo, Y. Boosting multimodal learning via disentangled gradient learning. In *Proceedings of the IEEE/CVF International Conference on Computer Vision*, pp. 22879–22888, 2025.

Wei, Y. and Hu, D. Mmpareto: Boosting multimodal learning with innocent unimodal assistance. *arXiv preprint arXiv:2405.17730*, 2024.

Wei, Y., Li, S., Feng, R., and Hu, D. Diagnosing and re-learning for balanced multimodal learning. In *European Conference on Computer Vision*, pp. 71–86. Springer, 2024.

Wu, M. and Goodman, N. Multimodal generative models for scalable weakly-supervised learning. *Advances in neural information processing systems*, 31, 2018.

Yang, Z., Li, W., Chen, H., Wang, P., Xiong, R., and Fan, X. Adaptive redundancy regulation for balanced multimodal information refinement. *arXiv preprint arXiv:2511.13755*, 2025.

Yaras, C., Chen, S., Wang, P., and Qu, Q. Explaining and mitigating the modality gap in contrastive multimodal learning. *arXiv preprint arXiv:2412.07909*, 2024.

Yi, L., Douady, R., and Chen, C. Decipher the modality gap in multimodal contrastive learning: From convergent representations to pairwise alignment. *arXiv preprint arXiv:2510.03268*, 2025.

Yin, W., Zhou, P., Xiao, Z., Liu, J., Yu, S., Sonke, J.-J., and Gavves, S. Towards uniformity and alignment for multimodal representation learning.

Yu, T., Kumar, S., Gupta, A., Levine, S., Hausman, K., and Finn, C. Gradient surgery for multi-task learning. *Advances in neural information processing systems*, 33: 5824–5836, 2020.

Zbontar, J., Jing, L., Misra, I., LeCun, Y., and Deny, S. Barlow twins: Self-supervised learning via redundancy reduction. In *International conference on machine learning*, pp. 12310–12320. PMLR, 2021.

Zong, D., Ding, C., Li, B., Li, J., and Zheng, K. Balancing multimodal learning via online logit modulation. In *Proceedings of the Thirty-Third International Joint Conference on Artificial Intelligence*, pp. 5753–5761, 2024.

Appendix	11
A Theory Proofs	11
A.1 Proof of Geometric Ambiguity	11
A.2 Proof of Lemma 3.1 (Repulsive Gradients of Dispersive Potentials)	12
A.3 Proof of Theorem 3.2 (Uniformity and Effective Rank)	13
A.4 Proof of Theorem 3.3 (Anchoring Bounds Cross-Modal Drift)	13
A.5 Moment-constrained maximum-entropy formulation.	15
B Implementations and Experiment Details	15
B.1 Datasets Introduction	15
B.2 Overall Training Procedure and Baseline Implementations	16
B.3 Training Environment and Computational Overhead	16
C Geometry Diagnostics and Visualizations	16
C.1 Unimodal Geometry and Cross-modal Drift Diagnostics	16
C.2 Cross-modal Similarity Distributions	18
C.3 Additional Feature Visualizations	18
D Additional Experiments	19
D.1 Hyper-parameter Sensitivity	19
D.2 Robustness to Missing or Corrupted Modalities	21
D.3 Additional Baselines Compared with Contrastive Learning on CREMA-D	22

A. Theory Proofs

Organization. This appendix provides formal proofs for the theoretical claims in Section 3: (i) geometric ambiguity under decoupled supervision, (ii) repulsive gradients induced by dispersive potentials (Lemma 3.1), (iii) RBF uniformity encourages high entropy and higher effective rank (Theorem 3.2), and (iv) anchoring bounds cross-modal drift up to an irreducible gap (Theorem 3.3).

A.1. Proof of Geometric Ambiguity

Let $\mathcal{L} = \sum_{m=1}^M \mathcal{L}_{\text{CE}}(W_m z^m, y)$ be the decoupled objective. If $\{z^m\}_{m=1}^M$ is an optimal solution, then there exists a family of orthogonal transformations $\{R_m\}_{m=1}^M$ such that $z'^m = R_m z^m$ is also optimal, provided each R_m preserves linear separability w.r.t. W_m

Proof. Fix a modality m and write $W := W_m \in \mathbb{R}^{K \times d}$, $z := z^m$. The loss $\mathcal{L}_{\text{CE}}(Wz, y)$ depends on z only through the logits $\ell = Wz$. Hence any transformation $z \mapsto z'$ satisfying $Wz' = Wz$ leaves the objective unchanged.

Let $\mathcal{N}(W) = \{v \in \mathbb{R}^d : Wv = 0\}$ be the null space. Choose orthonormal bases $V_0 \in \mathbb{R}^{d \times (d-r)}$ for $\mathcal{N}(W)$ and $V_1 \in \mathbb{R}^{d \times r}$ for $\mathcal{N}(W)^\perp$, where $r = \text{rank}(W)$. Stack $V = [V_1 \ V_0] \in \mathbb{R}^{d \times d}$, which is orthogonal, and note $WV_0 = 0$.

For any orthogonal matrix $Q \in \mathbb{R}^{(d-r) \times (d-r)}$, define

$$R := V_1 V_1^\top + V_0 Q V_0^\top. \quad (16)$$

Step 1: R is orthogonal. Using $V_1^\top V_0 = 0$, $V_1^\top V_1 = I$, $V_0^\top V_0 = I$, and $Q^\top Q = I$,

$$R^\top R = (V_1 V_1^\top + V_0 Q^\top V_0^\top)(V_1 V_1^\top + V_0 Q V_0^\top) \quad (17)$$

$$= V_1 V_1^\top + V_0 Q^\top Q V_0^\top \quad (18)$$

$$= V_1 V_1^\top + V_0 V_0^\top = I. \quad (19)$$

Step 2: R preserves logits, i.e., $WR = W$. Since $WV_0 = 0$,

$$WR = W(V_1 V_1^\top) + W(V_0 Q V_0^\top) \quad (20)$$

$$= W(V_1 V_1^\top) + (WV_0) Q V_0^\top \quad (21)$$

$$= W(V_1 V_1^\top). \quad (22)$$

Moreover, every $x \in \mathbb{R}^d$ decomposes as $x = V_1 V_1^\top x + V_0 V_0^\top x$ and $W(V_0 V_0^\top x) = 0$, so $Wx = W(V_1 V_1^\top x)$ for all x , which implies $W = W(V_1 V_1^\top)$. Hence $WR = W$.

Therefore, for any z , we have $W(Rz) = Wz$, and thus $\mathcal{L}_{\text{CE}}(W(Rz), y) = \mathcal{L}_{\text{CE}}(Wz, y)$. Applying the same construction independently to each modality yields $\{R_m\}_{m=1}^M$ with $W_m R_m = W_m$, so $\mathcal{L}(\{R_m z^m\}) = \mathcal{L}(\{z^m\})$. In particular, if $\{z^m\}$ is optimal, then $\{R_m z^m\}$ is also optimal. \square

A.2. Proof of Lemma 3.1 (Repulsive Gradients of Dispersive Potentials)

Lemma 3.1 (restated). Let $\{\tilde{z}_i\}_{i=1}^B \subset \mathbb{S}^{d-1}$ be ℓ_2 -normalized embeddings and define

$$L_{\text{disp}} = \frac{1}{B(B-1)} \sum_{i \neq j} \psi(\|\tilde{z}_i - \tilde{z}_j\|_2^2), \quad (23)$$

where $\psi : \mathbb{R}_{\geq 0} \rightarrow \mathbb{R}$ is non-increasing. Then for each i , any (sub)gradient admits

$$\nabla_{\tilde{z}_i} L_{\text{disp}} = \frac{2}{B(B-1)} \sum_{j \neq i} \psi'(\|\tilde{z}_i - \tilde{z}_j\|_2^2) (\tilde{z}_i - \tilde{z}_j), \quad (24)$$

where ψ' is the derivative when it exists (or any valid sub-derivative otherwise). Equivalently, the descent direction $-\nabla_{\tilde{z}_i} L_{\text{disp}}$ is a nonnegative weighted sum of $(\tilde{z}_i - \tilde{z}_j)$.

Proof. Fix i and denote $d_{ij} := \|\tilde{z}_i - \tilde{z}_j\|_2^2$. We first differentiate $d_{ij} = (\tilde{z}_i - \tilde{z}_j)^\top (\tilde{z}_i - \tilde{z}_j)$ w.r.t. \tilde{z}_i :

$$\nabla_{\tilde{z}_i} d_{ij} = 2(\tilde{z}_i - \tilde{z}_j).$$

For the pairwise term $\psi(d_{ij})$, the chain rule (or subgradient chain rule) gives

$$\nabla_{\tilde{z}_i} \psi(d_{ij}) = \psi'(d_{ij}) \nabla_{\tilde{z}_i} d_{ij} = 2\psi'(d_{ij})(\tilde{z}_i - \tilde{z}_j). \quad (25)$$

Summing over all $j \neq i$ and applying the prefactor yields the stated expression for $\nabla_{\tilde{z}_i} L_{\text{disp}}$.

Since ψ is non-increasing, any valid (sub)derivative satisfies $\psi'(u) \leq 0$. Defining $w_{ij} := -\psi'(d_{ij}) \geq 0$, we obtain

$$-\nabla_{\tilde{z}_i} L_{\text{disp}} = \frac{2}{B(B-1)} \sum_{j \neq i} w_{ij} (\tilde{z}_i - \tilde{z}_j), \quad (26)$$

which is a nonnegative weighted sum of directions pointing away from other samples. \square

Remark (sphere constraint). The expression above is the Euclidean gradient in \mathbb{R}^d . If optimizing directly on \mathbb{S}^{d-1} , one uses the Riemannian gradient obtained by projecting onto the tangent space at \tilde{z}_i ; the pairwise repulsive structure is preserved after projection.

A.3. Proof of Theorem 3.2 (Uniformity and Effective Rank)

Theorem 3.2 (restated). Let z be a random embedding on the unit sphere ($\|z\|_2 = 1$) with second moment $\Sigma = \mathbb{E}[zz^\top]$. Minimizing the dispersive loss

$$L_{\text{disp}} = \log \mathbb{E}[\exp(-t\|z - z'\|_2^2)], \quad z, z' \text{ i.i.d.},$$

is asymptotically equivalent to maximizing Rényi-2 entropy H_2 of the feature distribution. Moreover, uniformity minimization discourages anisotropy / low-rank covariance by reducing $\text{tr}(\Sigma^2)$ and thus increasing the effective rank $\text{Rank}_{\text{eff}}(\Sigma) = (\text{tr } \Sigma)^2 / \text{tr}(\Sigma^2)$.

Proof. **Part A: Rényi-2 interpretation (kernel viewpoint).** Let p be the feature distribution and define $k_t(z, z') = \exp(-t\|z - z'\|_2^2)$. Then

$$\mathbb{E}_{z, z' \sim p}[k_t(z, z')] = \iint p(z)p(z')k_t(z, z') dz dz'. \quad (27)$$

For a narrow kernel (bandwidth controlled by t), standard KDE arguments give $\mathbb{E}[k_t(z, z')] = C(t, d) \int p(z)^2 dz$ up to a multiplicative constant $C(t, d)$ independent of p . Since $H_2(p) = -\log \int p(z)^2 dz$, minimizing $L_{\text{disp}} = \log \mathbb{E}[k_t]$ is equivalent to maximizing $H_2(p)$ up to an additive constant.

Part B: Rewrite on the unit sphere. If $\|z\| = \|z'\| = 1$, then $\|z - z'\|_2^2 = 2 - 2z^\top z'$ and thus

$$k_t(z, z') = \exp(-2t) \exp(2t z^\top z').$$

Part C: Second-order expansion connects to $\text{tr}(\Sigma^2)$. Using $\exp(2tu) = 1 + 2tu + 2t^2u^2 + O(t^3)$ with $u = z^\top z'$ and taking expectations,

$$\mathbb{E}[k_t(z, z')] = \exp(-2t) \left(1 + 2t \mathbb{E}[z^\top z'] + 2t^2 \mathbb{E}[(z^\top z')^2] + O(t^3) \right).$$

If features are (approximately) centered so that $\mathbb{E}[z] = 0$, then by independence $\mathbb{E}[z^\top z'] = \mathbb{E}[z]^\top \mathbb{E}[z'] = 0$. For the quadratic term, using independence again,

$$\mathbb{E}[(z^\top z')^2] = \mathbb{E}[z^\top (z' z'^\top) z] = \mathbb{E}[z^\top \mathbb{E}[z' z'^\top] z] = \mathbb{E}[z^\top \Sigma z] = \text{tr}(\Sigma \mathbb{E}[zz^\top]) = \text{tr}(\Sigma^2).$$

Therefore, in the centered case,

$$\mathbb{E}[k_t(z, z')] = \exp(-2t) \left(1 + 2t^2 \text{tr}(\Sigma^2) + O(t^3) \right),$$

so minimizing $L_{\text{disp}} = \log \mathbb{E}[k_t]$ discourages large $\text{tr}(\Sigma^2) = \|\Sigma\|_F^2$, i.e., discourages anisotropy / low-rank covariance.

Part D: Effective rank. Define $\text{Rank}_{\text{eff}}(\Sigma) := (\text{tr } \Sigma)^2 / \text{tr}(\Sigma^2)$. On the unit sphere, $\text{tr } \Sigma = \mathbb{E}\|z\|_2^2 = 1$, hence

$$\text{Rank}_{\text{eff}}(\Sigma) = \frac{1}{\text{tr}(\Sigma^2)}.$$

Thus reducing $\text{tr}(\Sigma^2)$ increases $\text{Rank}_{\text{eff}}(\Sigma)$, pushing representations away from low-rank collapse. \square

A.4. Proof of Theorem 3.3 (Anchoring Bounds Cross-Modal Drift)

Theorem 3.3 (restated with a tolerance radius). Consider the joint objective

$$\mathcal{L}_{\text{total}} = \mathcal{L} + \lambda_{\text{inter}} \mathcal{L}_{\text{inter}} + \lambda_{\text{intra}} \mathcal{L}_{\text{intra}}, \quad (28)$$

where the bounded anchoring term is defined as

$$\mathcal{L}_{\text{inter}} := \mathbb{E} \left[(\|\tilde{z}^m - \tilde{z}^n\|_2 - \tau)_+^2 \right], \quad (x)_+ = \max(x, 0), \quad (29)$$

and $\tau \geq 0$ specifies a tolerance radius that preserves modality-specific deviations. Define the non-anchoring part of the objective as

$$\tilde{\mathcal{L}}(\tilde{z}^m, \tilde{z}^n) := \mathcal{L}(\tilde{z}^m, \tilde{z}^n) + \lambda_{\text{intra}} \mathcal{L}_{\text{intra}}(\tilde{z}^m, \tilde{z}^n). \quad (30)$$

We further define the *irreducible modality gap*

$$\delta := \min_{\tilde{z}} \tilde{\mathcal{L}}(\tilde{z}, \tilde{z}) - \min_{\tilde{z}^m, \tilde{z}^n} \tilde{\mathcal{L}}(\tilde{z}^m, \tilde{z}^n) \geq 0. \quad (31)$$

Let $(\tilde{z}_*^m, \tilde{z}_*^n)$ be a minimizer of $\mathcal{L}_{\text{total}}$. Then the expected *excess* cross-modal drift satisfies

$$\mathbb{E}[(\|\tilde{z}_*^m - \tilde{z}_*^n\|_2 - \tau)_+^2] \leq \frac{\delta}{\lambda_{\text{inter}}}. \quad (32)$$

Proof. By optimality of $(\tilde{z}_*^m, \tilde{z}_*^n)$, we have

$$\mathcal{L}_{\text{total}}(\tilde{z}_*^m, \tilde{z}_*^n) = \tilde{\mathcal{L}}(\tilde{z}_*^m, \tilde{z}_*^n) + \lambda_{\text{inter}} \mathbb{E}[(\|\tilde{z}_*^m - \tilde{z}_*^n\|_2 - \tau)_+^2] \quad (33)$$

$$\leq \min_{\tilde{z}} \left\{ \tilde{\mathcal{L}}(\tilde{z}, \tilde{z}) + \lambda_{\text{inter}} \mathbb{E}[(\|\tilde{z} - \tilde{z}\|_2 - \tau)_+^2] \right\}. \quad (34)$$

Since $\|\tilde{z} - \tilde{z}\|_2 = 0$ and $\tau \geq 0$, we have $(0 - \tau)_+ = 0$ and thus

$$\min_{\tilde{z}} \left\{ \tilde{\mathcal{L}}(\tilde{z}, \tilde{z}) + \lambda_{\text{inter}} \mathbb{E}[(\|\tilde{z} - \tilde{z}\|_2 - \tau)_+^2] \right\} = \min_{\tilde{z}} \tilde{\mathcal{L}}(\tilde{z}, \tilde{z}). \quad (35)$$

On the other hand, by definition of the minimum,

$$\tilde{\mathcal{L}}(\tilde{z}_*^m, \tilde{z}_*^n) \geq \min_{\tilde{z}^m, \tilde{z}^n} \tilde{\mathcal{L}}(\tilde{z}^m, \tilde{z}^n). \quad (36)$$

Combining the inequalities yields

$$\lambda_{\text{inter}} \mathbb{E}[(\|\tilde{z}_*^m - \tilde{z}_*^n\|_2 - \tau)_+^2] \leq \min_{\tilde{z}} \tilde{\mathcal{L}}(\tilde{z}, \tilde{z}) - \min_{\tilde{z}^m, \tilde{z}^n} \tilde{\mathcal{L}}(\tilde{z}^m, \tilde{z}^n) = \delta, \quad (37)$$

which completes the proof. \square

Corollary (overall drift bound). Although Theorem 3.3 bounds only the drift exceeding the tolerance radius τ , it also implies a bound on the overall cross-modal drift.

Corollary A.1. *Under the conditions of Theorem 3.3,*

$$\mathbb{E}[\|\tilde{z}_*^m - \tilde{z}_*^n\|_2^2] \leq 2\tau^2 + \frac{2\delta}{\lambda_{\text{inter}}}. \quad (38)$$

Proof. Let $d = \|\tilde{z}_*^m - \tilde{z}_*^n\|_2$. Since $d \leq \tau + (d - \tau)_+$, we have

$$d^2 \leq (\tau + (d - \tau)_+)^2 \leq 2\tau^2 + 2(d - \tau)_+^2, \quad (39)$$

where the last inequality uses $(a + b)^2 \leq 2a^2 + 2b^2$. Taking expectations and applying Theorem 3.3 yields

$$\mathbb{E}[d^2] \leq 2\tau^2 + 2\mathbb{E}[(d - \tau)_+^2] \leq 2\tau^2 + \frac{2\delta}{\lambda_{\text{inter}}} \rightarrow 2\tau^2 (\delta \rightarrow 0), \quad (40)$$

which completes the proof. \square

Interpretation. The quantity δ captures the unavoidable benefit of allowing modality-specific deviations, for instance due to modality-dependent noise or nuisance factors. Consequently, even at the optimum, a non-zero cross-modal drift is permitted, which is consistent with Remark 3.4.

Corollary A.2 (Average pairwise drift for M modalities). *Let*

$$\mathcal{L}_{\text{inter}} = \mathbb{E}\left[\frac{1}{M(M-1)} \sum_{m \neq n} \|\tilde{z}^m - \tilde{z}^n\|_2^2\right],$$

and define $\delta := \min_{\tilde{z}} \tilde{\mathcal{L}}(\tilde{z}, \dots, \tilde{z}) - \min_{\{\tilde{z}^m\}} \tilde{\mathcal{L}}(\{\tilde{z}^m\}) \geq 0$, where $\tilde{\mathcal{L}}$ denotes the objective without $\mathcal{L}_{\text{inter}}$ and the tied set is $\tilde{z}^1 = \dots = \tilde{z}^M = \tilde{z}$. Let $\{\tilde{z}_*^m\}_{m=1}^M$ minimize $\tilde{\mathcal{L}}(\{\tilde{z}^m\}) + \lambda_{\text{inter}} \mathcal{L}_{\text{inter}}$. Then

$$\mathbb{E}\left[\frac{1}{M(M-1)} \sum_{m \neq n} \|\tilde{z}_*^m - \tilde{z}_*^n\|_2^2\right] \leq \frac{\delta}{\lambda_{\text{inter}}} + 2\tau^2.$$

Proof. Identical to Theorem 3.3 by comparing the optimum to the tied family, for which $\mathcal{L}_{\text{inter}} = 0$. \square

A.5. Moment-constrained maximum-entropy formulation.

Let $\tilde{z}^m = f_m(x^m; \theta)$ denote the ℓ_2 -normalized embedding of modality m , which induces a random variable Z_θ^m supported on the unit hypersphere. We aim to maximize unimodal representation diversity while bounding excessive cross-modal drift. For simplicity, we present the constraint for a modality pair (m, n) ; in practice, it can be enforced for each pair or averaged over pairs.

$$\max_{\theta} \sum_{m=1}^M H_2(Z_\theta^m) \quad \text{s.t.} \quad \mathbb{E} \left[(\|\tilde{z}^m - \tilde{z}^n\|_2 - \tau)_+^2 \right] \leq \epsilon, \quad (41)$$

where $H_2(\cdot)$ denotes the Rényi-2 entropy and ϵ specifies a drift budget.

Eq. (41) admits the Lagrangian

$$\mathcal{J}(\theta, \lambda_{\text{inter}}) = - \sum_{m=1}^M H_2(Z_\theta^m) + \lambda_{\text{inter}} \left(\mathbb{E} \left[(\|\tilde{z}^m - \tilde{z}^n\|_2 - \tau)_+^2 \right] - \epsilon \right), \quad \lambda_{\text{inter}} \geq 0, \quad (42)$$

where λ_{inter} is the dual variable associated with the drift budget.

Dropping the constant term $-\lambda_{\text{inter}}\epsilon$ and invoking Thm. 3.2, maximizing $H_2(Z_\theta^m)$ can be achieved by minimizing an RBF-based uniformity surrogate $\mathcal{L}_{\text{uni}}^m(\theta)$. Consequently, optimizing DAGR corresponds to minimizing a surrogate objective of Eq. (42):

$$\min_{\theta} \lambda_{\text{intra}} \sum_{m=1}^M \mathcal{L}_{\text{uni}}^m(\theta) + \lambda_{\text{inter}} \mathbb{E} \left[(\|\tilde{z}^m - \tilde{z}^n\|_2 - \tau)_+^2 \right], \quad (43)$$

which recovers the proposed intra-modal dispersive regularization and bounded inter-modal anchoring term.

B. Implementations and Experiment Details

B.1. Datasets Introduction

CREMA-D (Cao et al., 2014) is an audio–visual dataset designed for speech emotion recognition, which contains 7,442 short video clips of 2–3 seconds performed by 91 actors, annotated with 6 emotion categories. Following prior work, we randomly split the dataset into 6,698 samples for training and 744 samples for testing. This dataset evaluates the model’s ability to learn complementary audio and visual representations under relatively balanced modalities.

Kinetics-Sounds (KS) (Arandjelovic & Zisserman, 2017) is an audio–visual dataset constructed by filtering the Kinetics dataset to retain 34 sound-related action classes that are potentially manifested in both visual and auditory channels. It contains approximately 19k 10-second video clips, with 15k samples for training, 1.9k for validation, and 1.9k for testing. Compared to CREMA-D, KS presents a more challenging setting due to higher intra-class diversity and frequent modality imbalance, making it suitable for evaluating robustness under complex multimodal interactions.

CUB Image-Captions for Clustering (CUBICC) is a bimodal image–text dataset derived from the CUB image caption dataset constructed by Palumbo *et al.* (Palumbo et al., 2024), consisting of bird images paired with corresponding natural language descriptions. The dataset is organized into 8 semantic categories based on bird species, which is adopted to evaluate the model’s ability to disentangle and align multimodal latent spaces under fine-grained semantic supervision, rather than to exhaustively cover all possible modality combinations.

XRF55 (Wang et al., 2024a) is a large-scale multi-RF dataset for indoor human action recognition. It contains 42.9K synchronized samples spanning 55 action classes, collected from 39 subjects over 100 days. Each sample consists of multiple radio-frequency sensing modalities, including Wi-Fi CSI (9 links), RFID phase sequences (23 tags), and mmWave radar measurements, together with synchronized Azure Kinect recordings (RGB, depth, and infrared). Following the official protocol, we use the first 14 trials of each action performed by each subject for training and the remaining 6 trials for testing, resulting in 30.0K training samples and 12.9K test samples. This dataset allows us to evaluate whether DAGR generalizes beyond conventional audio–visual settings to privacy-preserving RF-based multimodal perception with heterogeneous sensing modalities.

Table 5. Training time and computational overhead under different batch sizes on CREMA-D and Kinetics-Sounds. All experiments are conducted on a single NVIDIA H100 GPU.

Batch Size	CREMA-D			Kinetics-Sounds		
	Baseline (s)	Baseline + DAGR (s)	Over. (%)	Baseline (s)	Baseline + DAGR (s)	Over. (%)
32	22.36	25.80	+15.4	89.49	102.67	+14.7
64	21.19	23.83	+12.5	86.63	95.03	+9.7
128	21.03	23.55	+12.0	FAILED ¹	FAILED ¹	—
256	21.02	22.95	+9.2	FAILED ¹	FAILED ¹	—

B.2. Overall Training Procedure and Baseline Implementations

We incorporate DAGR into the original training objective in a plug-and-play manner, without modifying the backbone architectures or optimization pipeline. Specifically, the overall training loss is defined as

$$\mathcal{L}_{\text{total}} = \mathcal{L} + \mathcal{L}_{\text{DAGR}}, \quad (44)$$

where \mathcal{L} denotes the original task-specific objective (e.g., cross-entropy), and $\mathcal{L}_{\text{DAGR}}$ is applied as an auxiliary regularization term on the intermediate modality embeddings.

Baseline implementation and fairness settings. For all baseline methods, we adopt identical data splits, feature extractors, backbone architectures, batch sizes, optimizers, and learning-rate schedules. Only method-specific components (e.g., gradient modulation, objective reweighting, or fusion strategies) are changed to ensure a fair comparison.

Implementation details of baseline methods. Whenever available, we rely on official implementations or publicly released benchmark codebases. If an official implementation is not available, we re-implement the method following the original paper and match the reported hyper-parameters as closely as possible. For all baselines and their corresponding variants augmented with DAGR, we run experiments with three different random seeds (0, 42, 3407) and report the mean and standard deviation of the results.

B.3. Training Environment and Computational Overhead

All experiments were conducted on a server equipped with a single NVIDIA H100 GPU with 80 GB of VRAM and 128 GB of system memory. Unless otherwise specified, all models were trained and evaluated under identical hardware, software, and optimization settings to ensure fair runtime comparisons.

DAGR is implemented as a lightweight regularization module applied to intermediate modality embeddings and introduces no additional trainable parameters. Its intra-modal dispersion term requires pairwise distance computations within each modality, while the inter-modal anchoring term enforces sample-level alignment across modalities. Both terms are implemented using fully vectorized tensor operations and are activated only during training, incurring no additional cost at inference time.

Table 5 and 6 reports the average per-epoch training time on representative benchmarks, comparing the baseline models with their counterparts augmented by DAGR. Across datasets of different scales and modality compositions, DAGR introduces only a modest increase in training time, remaining well within practical limits on modern GPU hardware.

C. Geometry Diagnostics and Visualizations

C.1. Unimodal Geometry and Cross-modal Drift Diagnostics

Goal and setup. We report training-time geometric diagnostics to validate the behaviors predicted by our analysis. We compare three variants: (i) **Baseline**; (ii) **Disp Only** (baseline augmented with the dispersion term only); and (iii) **Ours** (baseline augmented with DAGR, instantiated as Pareto+Hinge). All curves are plotted over training epochs.

¹**FAILED:** CUDA OOM in the baseline at this batch size (NVIDIA H100, 80 GB VRAM, AMP enabled). Results at smaller batch sizes confirm DAGR adds <15% overhead on average.

Table 6. Training time and computational overhead under different batch sizes on XRF55 and CUBICC. All experiments are conducted on a single NVIDIA H100 GPU.

Batch Size	XRF55			CUBICC		
	Baseline (s)	Baseline + DAGR (s)	Over. (%)	Baseline (s)	Baseline + DAGR (s)	Over. (%)
32	258.23	272.38	+5.19	68.26	78.85	+15.5
64	255.55	257.78	+0.87	64.84	71.66	+10.5
128	247.12	248.46	+0.54	71.31	76.44	+7.2
256	246.26	244.23	-0.82	FAILED ¹	FAILED ¹	-

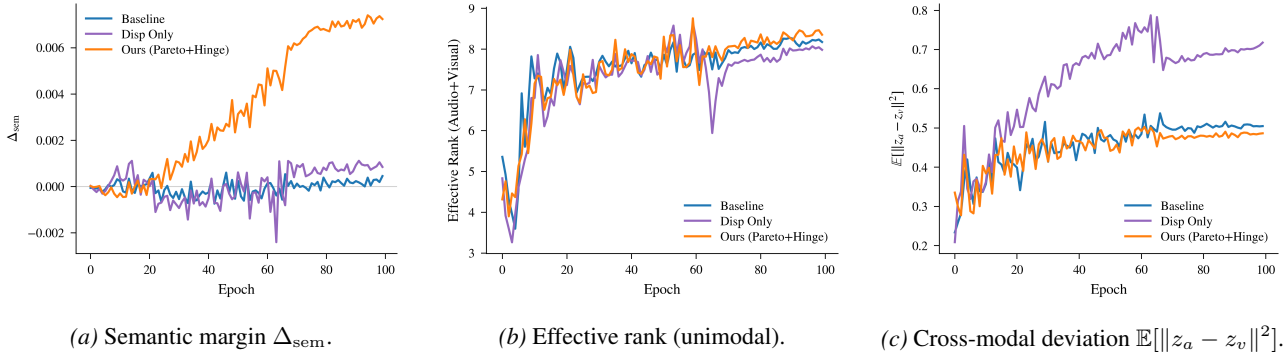


Figure 2. Training-time geometric diagnostics. **Left:** semantic margin Δ_{sem} (Eq. 45), where DAGR steadily improves semantic separability compared with both the baseline and Disp Only. **Middle:** effective rank of unimodal representations, showing that dispersion increases intrinsic dimensionality. **Right:** cross-modal deviation converging to a non-zero plateau, consistent with an irreducible modality gap; DAGR achieves more stable alignment than dispersion alone.

Semantic margin Δ_{sem} . To quantify semantic separability of the learned representations, we define the *semantic margin* Δ_{sem} as the difference between the average inter-class distance and the average intra-class distance in the representation space:

$$\Delta_{\text{sem}} = \mathbb{E}_{y \neq y'} \left[\mathbb{E}_{i \in \mathcal{I}_y, j \in \mathcal{I}_{y'}} \|z_i - z_j\|_2 \right] - \mathbb{E}_y \left[\mathbb{E}_{i, j \in \mathcal{I}_y} \|z_i - z_j\|_2 \right], \quad (45)$$

where \mathcal{I}_y is the index set of samples with class label y , and z denotes the representation used for evaluation. A larger Δ_{sem} indicates better class-wise separation.

Diagnostics and observations. As shown in Figure 2(a), DAGR yields a steadily increasing Δ_{sem} during training, indicating improved semantic separability compared with both the baseline and Disp Only. Interestingly, Disp Only exhibits noticeably higher variance and can even reduce Δ_{sem} at certain stages, suggesting that dispersion alone may enlarge the representation spread without consistently enhancing class separation. In contrast, DAGR improves separability more reliably, consistent with our geometry-aware objective.

Figure 2(b) tracks the intrinsic dimensionality of unimodal representations via effective rank (higher implies less collapsed and more diversified features). Both Disp Only and DAGR maintain competitive or improved effective rank relative to the baseline throughout training, supporting the claim that dispersion promotes richer unimodal geometry (cf. Theorem 3.2). Notably, DAGR achieves this while simultaneously improving Δ_{sem} , suggesting a better trade-off than dispersion alone.

Finally, Figure 2(c) plots the cross-modal deviation $\mathbb{E}[\|z_a - z_v\|^2]$ (audio vs. visual; adapt modalities as needed). All methods converge to a non-zero plateau rather than vanishing to zero, which is consistent with an irreducible modality gap arising from modality-specific noise, aligned with the non-zero δ in Theorem 3.3. Compared with the baseline, DAGR attains a slightly lower (or comparable) deviation level while avoiding the instability seen in Disp Only, indicating improved anchoring without forcing unrealistic perfect matching.

C.2. Cross-modal Similarity Distributions

To further analyze how geometry-aware regularization affects cross-modal alignment at the sample level, we examine the distribution of cosine similarities between cross-modal embedding pairs. Specifically, we consider *positive* pairs, where embeddings from different modalities correspond to the same sample, and *negative* pairs formed by randomly mismatched samples. All similarities are computed using ℓ_2 -normalized intermediate embeddings.

Distributional separation metrics. To quantitatively assess the separability between the similarity distributions of positive and negative pairs, we report two complementary metrics that capture different aspects of distributional difference.

First, we measure the mean similarity gap

$$\Delta\mu := \mathbb{E}[s_{\text{pos}}] - \mathbb{E}[s_{\text{neg}}], \quad (46)$$

where s_{pos} and s_{neg} denote the cosine similarities of positive and negative pairs, respectively. This metric characterizes the first-order (mean-level) separation between the two distributions. A larger $\Delta\mu$ indicates that, on average, positive pairs are assigned higher similarity scores than negative pairs, reflecting improved global discrimination.

However, mean separation alone does not fully describe how well the two distributions are distinguished. Two distributions may have similar means yet differ substantially in dispersion, overlap, or tail behavior. To capture such effects, we additionally report the Kolmogorov–Smirnov (KS) distance D_{KS} between the empirical distributions of s_{pos} and s_{neg} . The KS distance is defined as the maximum absolute difference between their cumulative distribution functions,

$$D_{\text{KS}} = \sup_x |F_{\text{pos}}(x) - F_{\text{neg}}(x)|, \quad (47)$$

where F_{pos} and F_{neg} denote the empirical CDFs of positive and negative similarities, respectively.

Unlike $\Delta\mu$, which summarizes only the average separation, D_{KS} measures the largest distributional discrepancy at any similarity threshold. It is sensitive to higher-order characteristics such as variance, skewness, and tail overlap, and therefore provides a more holistic view of how well the two similarity distributions are separated across their entire support. Together, $\Delta\mu$ and D_{KS} offer complementary perspectives on distributional separability, capturing both mean-level and shape-level differences.

Observed effects of geometry-aware regularization. As shown in Fig. 3(a), the baseline exhibits highly overlapping similarity distributions for positive and negative pairs, indicating weak cross-modal discriminability. This is reflected by a near-zero mean gap ($\Delta\mu = +0.00061$) and a small KS distance ($D_{\text{KS}} = 0.02577$), suggesting that matched pairs are not consistently ranked above mismatched ones.

After incorporating dispersion together with alignment/anchoring (Fig. 3(b)), the positive and negative distributions become substantially more separated. Both the mean gap ($\Delta\mu = +0.01415$) and the KS distance ($D_{\text{KS}} = 0.09267$) increase markedly, indicating improved cross-modal discriminability. This behavior is consistent with the intended effect of the regularizer: dispersion prevents representation collapse, while anchoring reduces sample-level cross-modal drift, jointly reshaping the similarity geometry.

Implications for retrieval. Finally, Fig. 3(c) reports retrieval-style performance measured by Recall@K, which evaluates the probability that a true cross-modal match appears among the top- K retrieved candidates. Consistent with the improved distributional separation, the regularized model achieves higher Recall@K across a wide range of K , with especially pronounced gains for larger K . This suggests that the learned similarity geometry not only improves average separability, but also yields more favorable global ranking behavior for cross-modal retrieval.

C.3. Additional Feature Visualizations

To qualitatively examine the effect of geometry-aware regularization on multimodal representation structure, we provide additional 2D visualizations on three datasets: CREMA-D, CUB Image-Captions for Clustering (CUBICC), and XRF55. For each dataset, we project intermediate multimodal embeddings into two dimensions using t-SNE (or PCA when specified), where each point corresponds to a single sample and colors denote semantic categories. For paired modalities (e.g., audio–visual or image–caption), samples from the same instance share the same label, allowing us to inspect cross-modal consistency.

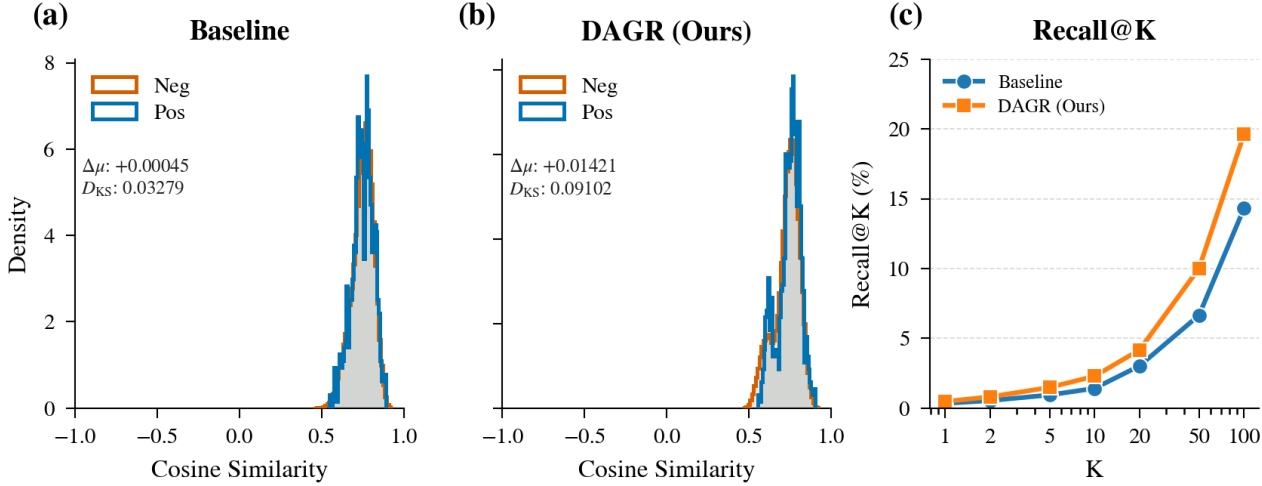


Figure 3. Cross-modal similarity geometry. (a) Cosine similarity distributions between positive (matched) and negative (mismatched) cross-modal pairs under the DGL baseline. (b) The corresponding distributions after adding a dispersive loss with an alignment/anchoring component, showing increased separation (larger $\Delta\mu$ and D_{KS}). (c) Retrieval performance measured by Recall@K, where improved separability translates into higher recall.

CREMA-D. Figure 4 visualizes multimodal embeddings on CREMA-D. The baseline exhibits noticeable overlap between emotion categories and fragmented cluster structure, with limited alignment between paired modalities. In contrast, incorporating geometry-aware regularization leads to more compact class-wise clusters and improved co-localization of audio and visual embeddings within each emotion category, indicating enhanced intra-modal structure and more stable cross-modal consistency.

CUBICC. Figure 5 shows the visualization results on the CUBICC dataset. While the baseline already exhibits partial semantic separation, image and caption embeddings of the same category often form loosely overlapping or fragmented structures. With geometry-aware regularization, clusters become more coherent and better separated, and paired image-caption embeddings display improved overlap within each semantic category, suggesting enhanced semantic organization without enforcing rigid global alignment.

XRF55. Figure 6 presents the visualization on the XRF55 dataset. The baseline representations show substantial inter-class mixing and inconsistent cross-modal alignment. After applying geometry-aware regularization, semantic clusters become more distinguishable, and paired modalities exhibit clearer co-localization, reflecting improved representation geometry under higher noise and heterogeneity.

We emphasize that these visualizations are intended for qualitative inspection only and do not fully capture the high-dimensional geometry. Nevertheless, the observed trends are consistent across datasets and align with the quantitative improvements reported in clustering performance and geometric diagnostics (Appendix C.1).

D. Additional Experiments

D.1. Hyper-parameter Sensitivity

Our method introduces two weighting coefficients, λ_{intra} and λ_{inter} , to balance intra-modal compactness and inter-modal alignment. In principle, tuning these two hyper-parameters also depends on the hinge loss threshold τ , since the effective contribution of the hinge term is jointly determined by both the margin τ and the loss weights. As a result, naively performing a grid search over $(\lambda_{\text{intra}}, \lambda_{\text{inter}}, \tau)$ would lead to a large and unstable hyper-parameter space.

Sensitivity to λ_{intra} and λ_{inter} . To first isolate the effect of the two weighting coefficients, we fix the hinge threshold to $\tau = 0$ and conduct a two-dimensional grid search over $(\lambda_{\text{intra}}, \lambda_{\text{inter}})$. Figure 7 shows the resulting performance heatmaps on CREMA-D and Kinetics-Sound.

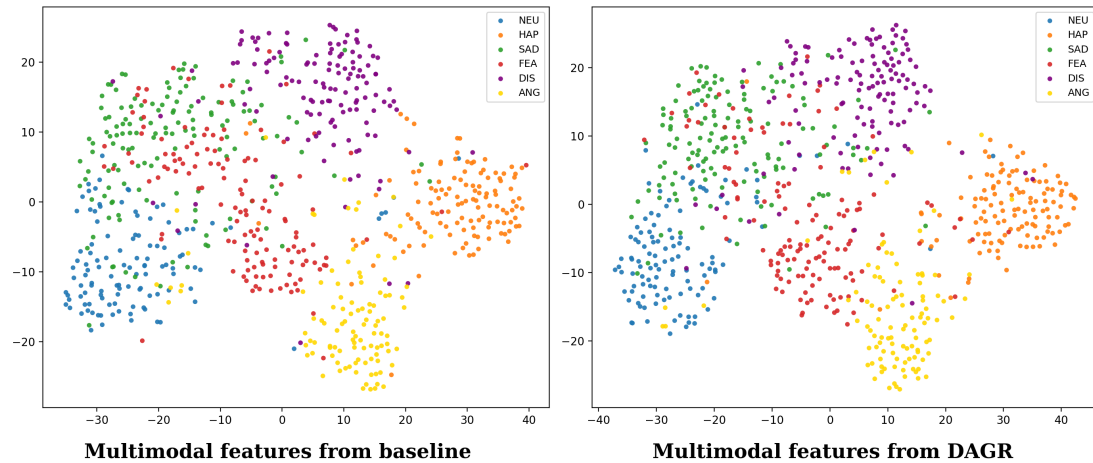


Figure 4. t-SNE visualization of multimodal embeddings on CREMA-D. DAGR produces more compact and better-aligned semantic clusters compared with the baseline.

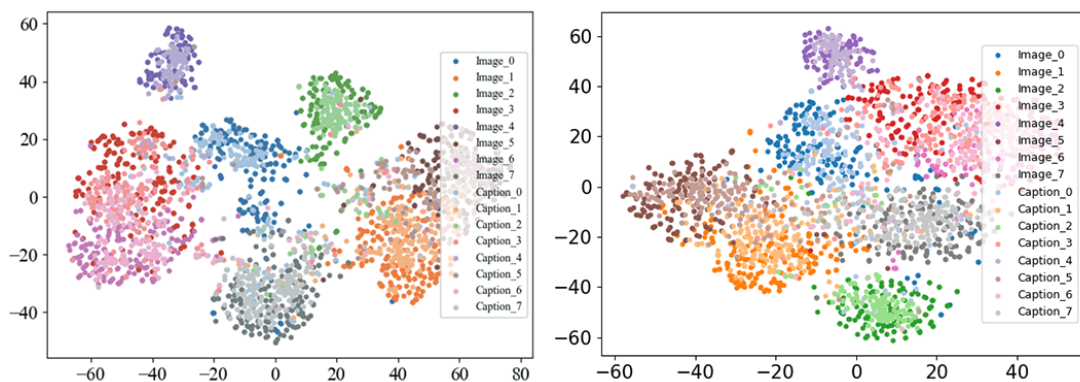


Figure 5. t-SNE visualization of multimodal embeddings on CUBICC. DAGR improves semantic compactness and stabilizes image–caption alignment relative to the baseline.

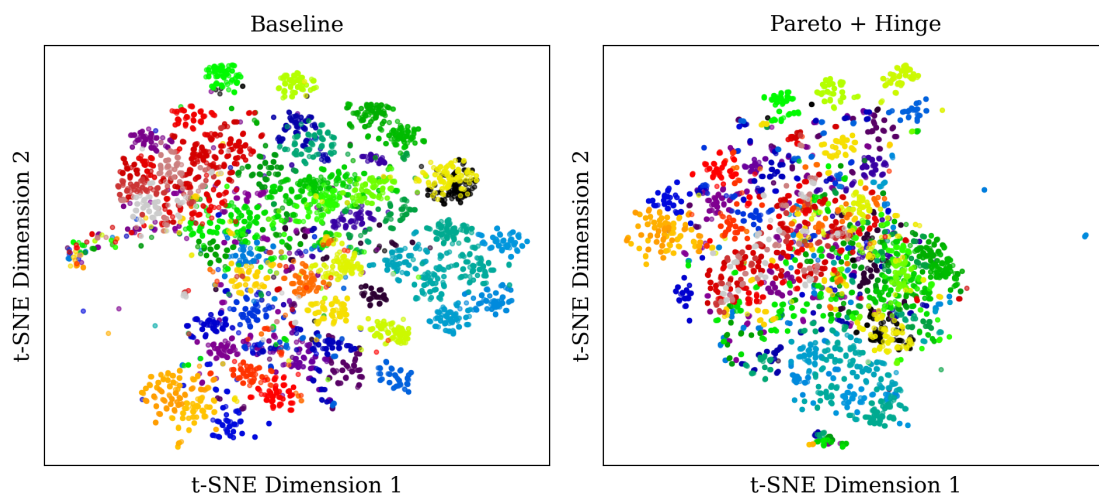


Figure 6. t-SNE/PCA visualization of multimodal embeddings on X-Fi. DAGR yields clearer cluster separation and more consistent cross-modal structure.

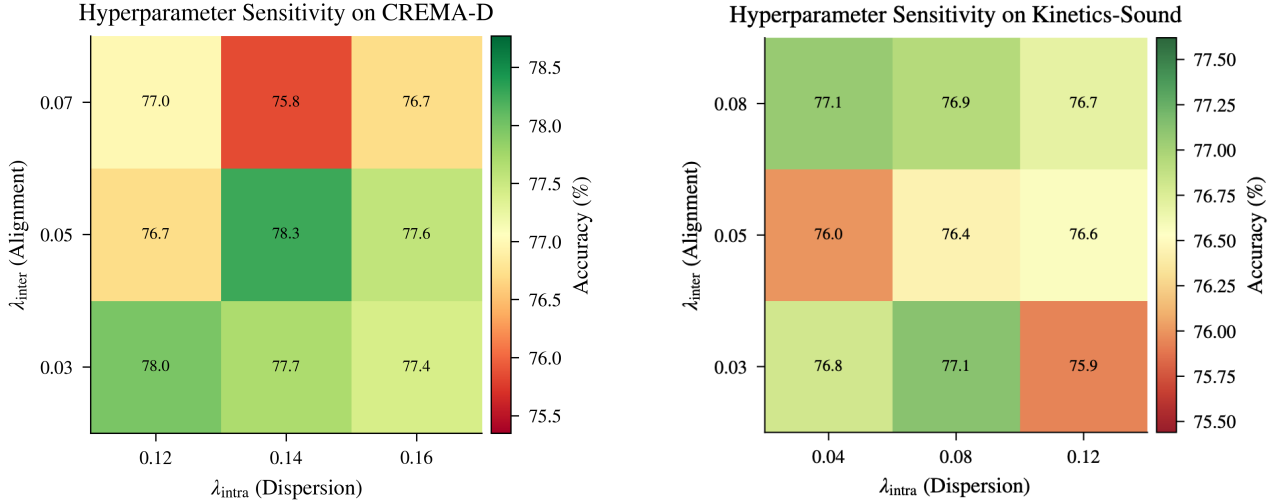


Figure 7. Sensitivity analysis of λ_{intra} and λ_{inter} with the hinge threshold fixed to $\tau = 0$. Left: CREMA-D. Right: Kinetics-Sound.

From the results, we observe that moderate values of both λ_{intra} and λ_{inter} generally lead to better performance, while overly large weights do not consistently improve accuracy. This suggests that excessively emphasizing the auxiliary contrastive objectives may dominate the optimization process and suppress task-relevant discriminative cues learned by the primary classification loss. Moreover, strong intra-/inter-regularization may over-constrain the feature geometry, reducing representation flexibility and harming generalization.

Joint sensitivity of β and τ . Motivated by the above observations, we further adopt a Pareto-style parameterization that controls the total regularization strength using a single scalar $\beta = \lambda_{\text{intra}} + \lambda_{\text{inter}}$, while maintaining a balanced trade-off between intra-modal compactness and inter-modal alignment. Specifically, we consider $\beta \in \{0.1, 0.15, 0.2\}$, which significantly reduces the hyper-parameter search space and improves training stability.

We then conduct an ablation study on the hinge threshold $\tau \in \{0, 0.25, 0.5\}$ under different values of β . Figure 8 visualizes the joint sensitivity of β and τ on CREMA-D and Kinetics-Sound. Overall, the results indicate that our method is relatively robust to moderate variations of τ , while excessively large margins may degrade performance when combined with strong regularization. This further supports our choice of using a small β together with a mild hinge threshold.

D.2. Robustness to Missing or Corrupted Modalities

We further evaluate DAGR under *test-time modality degradation* to directly validate the motivation in Sec. 1: when one modality becomes partially missing or corrupted, a robust multimodal model should degrade *gracefully*. Unless otherwise specified, we corrupt *only one* modality at a time during inference while keeping all other modalities unchanged.

CREMA-D: missing and corruption stress tests. For the audio-visual setting on CREMA-D, we consider both *missingness* and *sensor-like corruptions*. (i) **Random missingness.** With probability $p \in [0, 1]$, we replace a modality with a missing placeholder at test time (feature-level masking), resulting in missing-audio and missing-visual curves. (ii) **Audio noise.** We inject additive noise with different SNR levels (dB) to simulate degraded audio acquisition. (iii) **SpecAugment / frame-drop / cutout.** We apply standard modality-specific corruptions: SpecAugment masks a fraction of time/frequency bins on audio features, frame-drop randomly removes a fraction of frames from the visual stream, and cutout occludes a random rectangular region with a given area ratio.

X-FI: dropout corruption. We first evaluate robustness to *partial feature loss* by progressively applying random dropout to a single modality at test time, while keeping all other modalities unchanged. Specifically, for the selected modality we randomly mask a fraction ρ of its feature dimensions or tokens (drop ratio $\rho \in [0, 1]$) before inference. This setting simulates scenarios where a modality is only partially available due to occlusion, packet loss, or unstable sensing.

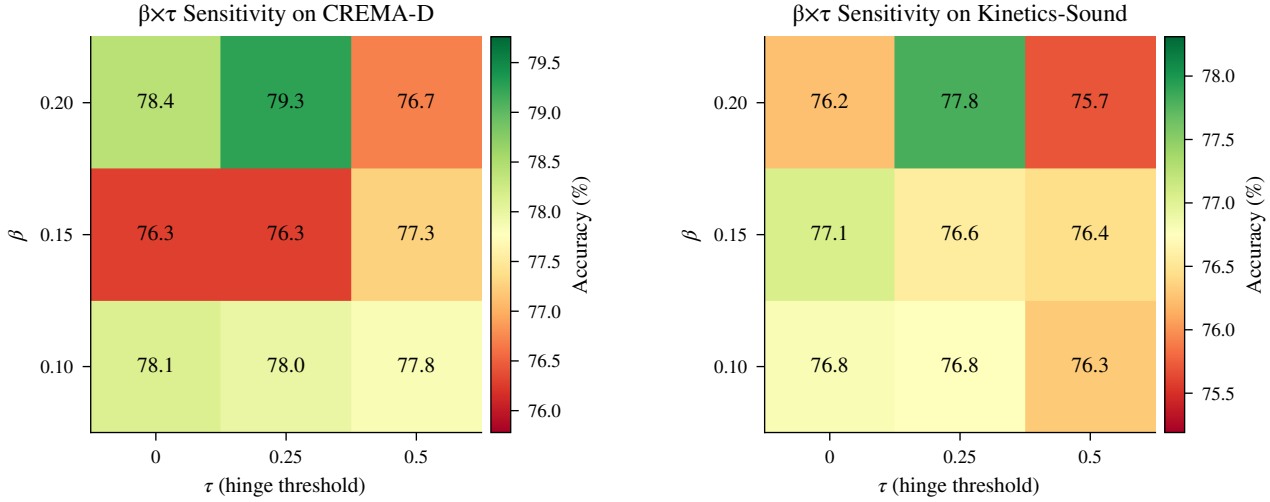


Figure 8. Joint sensitivity analysis of total regularization strength β and hinge threshold τ across two datasets. Left: CREMA-D. Right: Kinetics-Sound.

X-FI: Gaussian corruption. Next, we study robustness to *additive sensor noise* by injecting Gaussian noise into one modality at test time. For modality m , the corrupted input is constructed as $\tilde{\mathbf{x}}^{(m)} = \mathbf{x}^{(m)} + \sigma \cdot s^{(m)} \epsilon$, where $\epsilon \sim \mathcal{N}(0, 1)$, σ controls the noise strength, and $s^{(m)}$ is a modality-specific scale to normalize noise magnitude across modalities. We sweep σ from weak to strong corruption and report the resulting degradation curves.

X-FI: random missingness. Finally, we evaluate robustness to *temporal or segment-level modality absence* by randomly masking parts of a modality. Concretely, for the selected modality, each temporal step or segment is independently removed with probability p (drop rate $p \in [0, 1]$), while all other modalities remain intact. This setting simulates intermittent sensor failures or missing data streams, which are common in real-world deployments.

Discussion. Fig. 9 and Figs. 10–12 provide a direct robustness diagnosis beyond standard unimodal ablations. Across datasets, performance degrades monotonically as corruption severity increases, validating these perturbations as meaningful stress tests. Overall, DAGR tends to achieve higher accuracy and smoother degradation trends when a single modality becomes unreliable, indicating improved robustness of multimodal fusion.

On X-FI, the gains are particularly pronounced for mmWave and WiFi under moderate-to-severe corruption, where the baseline suffers sharper drops. For RFID, partially corrupted inputs can be more harmful than fully missing ones, suggesting that misleading low-quality signals may interfere with fusion; in these regimes, DAGR maintains a clearer advantage, consistent with stronger resistance to unreliable modality information. On CREMA-D, DAGR improves robustness in the low-to-moderate degradation regime across multiple corruption types and remains competitive under severe corruption, supporting the claim that DAGR alleviates geometric pathologies that otherwise amplify sensitivity to modality degradation.

D.3. Additional Baselines Compared with Contrastive Learning on CREMA-D

Setup. We report results on CREMA-D with four additional controls designed to disentangle the effects of (i) always-on cross-modal coupling (naive alignment), (ii) redundancy-reduction objectives commonly used in non-contrastive/self-supervised learning (VICReg-/Barlow-style), and (iii) feature normalization alone (unit-sphere projection). All methods use the same backbone, optimization schedule, and evaluation protocol as in the main experiments; only the specified regularization term or normalization operation is changed.

Results and Discussion. As shown in Table 7, **naive alignment** and **VICReg-style** regularization achieve competitive multimodal accuracy (77.98 and 78.12), but their improvements do not translate into consistently stronger unimodal performance: VICReg-style notably underperforms on audio (59.18), and naive alignment, while boosting the visual branch (72.21), yields a smaller gain on audio (60.65). In contrast, **our method** attains the best multimodal accuracy (78.16) and

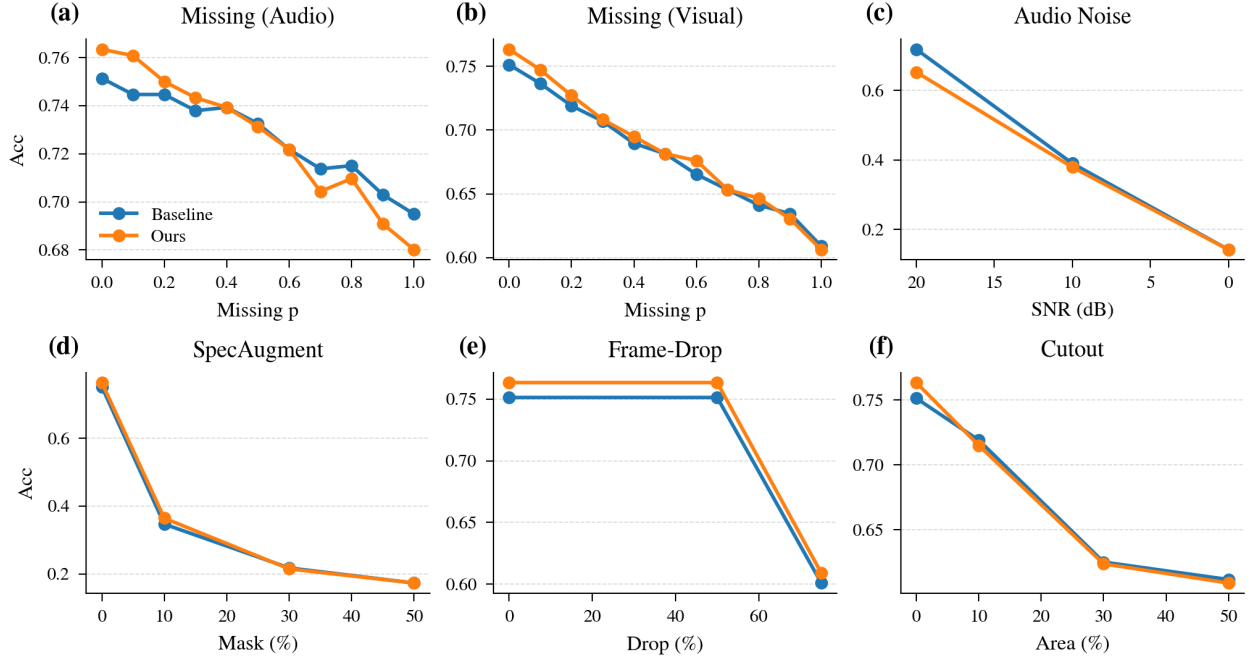


Figure 9. Robustness under missing or corrupted modalities on CREMA-D. We evaluate test-time degradation by (a) missing audio, (b) missing visual, (c) additive audio noise (SNR sweep), and modality-specific corruptions including (d) SpecAugment, (e) frame-drop, and (f) cutout. DAGR generally exhibits improved robustness in the low-to-moderate degradation regime and maintains competitive performance under severe corruption, yielding smoother degradation trends than the baseline.

the best audio accuracy (62.98), while remaining competitive on visual (72.10). This pattern supports our motivation that *always-on invariance/coupling* can over-constrain modality-specific features, whereas our bounded anchoring combined with dispersive regularization better preserves modality-unique information while still improving cross-modal fusion. Finally, the **unit-sphere only** control provides limited gains (75.81 multimodal), suggesting that the improvement is not explained by normalization alone but requires explicit geometric regularization.

Why our regularization is not contrastive learning. It is important to distinguish our objective from contrastive (InfoNCE-style) learning and invariance-driven paired objectives. Contrastive learning performs *instance discrimination* by comparing each positive pair against a set of negatives, e.g.,

$$\mathcal{L}_{\text{InfoNCE}} = -\mathbb{E}_i \log \frac{\exp(\text{sim}(\mathbf{z}_i^{(a)}, \mathbf{z}_i^{(v)})/t)}{\sum_j \exp(\text{sim}(\mathbf{z}_i^{(a)}, \mathbf{z}_j^{(v)})/t)}, \quad (48)$$

which *always* increases the positive similarity while *repelling* all other instances. In contrast, our anchoring term is *bounded* and does not enforce global invariance:

$$\mathcal{L}_{\text{anchor}} = \mathbb{E}_i \left[\left(\left\| \tilde{\mathbf{z}}_i^{(a)} - \tilde{\mathbf{z}}_i^{(v)} \right\|_2 - \tau \right)_+^2 \right]. \quad (49)$$

Its gradient is *exactly zero* whenever $\|\tilde{\mathbf{z}}_i^{(a)} - \tilde{\mathbf{z}}_i^{(v)}\|_2 \leq \tau$, meaning we do not keep pulling paired embeddings together once they are within an acceptable deviation band. Therefore, our method is not a contrastive objective (no negatives, no softmax normalization), and it is not a pure invariance constraint either.

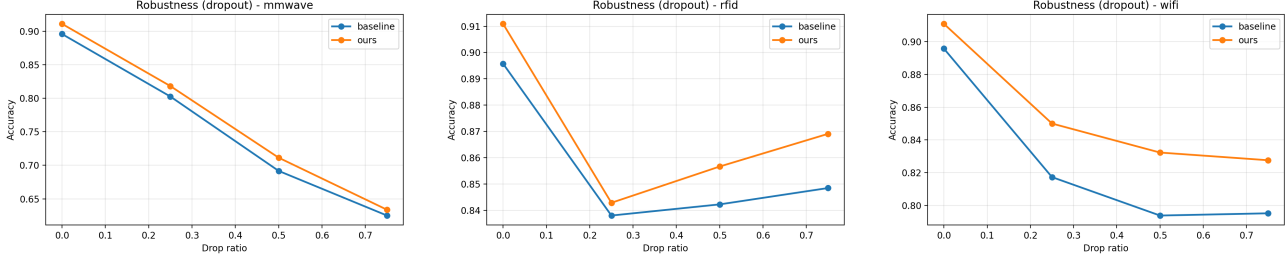


Figure 10. Robustness under dropout on X-FI. We progressively drop a fraction ρ of features from one modality at test time, while keeping the other modalities intact. From left to right: mmWave, RFID, and WiFi. DAGR attains higher accuracy and degrades more gracefully than the baseline, especially under moderate-to-severe dropout.

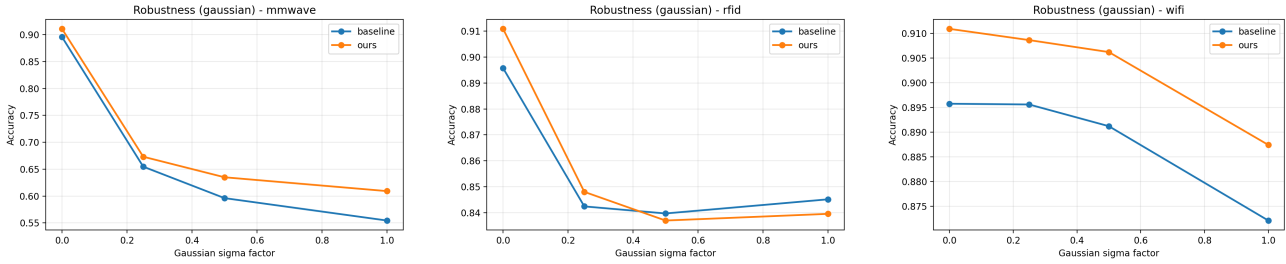


Figure 11. Robustness under Gaussian noise on X-FI. We inject additive Gaussian noise with factor σ into a single modality at test time. From left to right: mmWave, RFID, and WiFi. DAGR shows improved robustness under noisy inputs (notably for mmWave and WiFi) and generally degrades more smoothly than the baseline as noise increases.

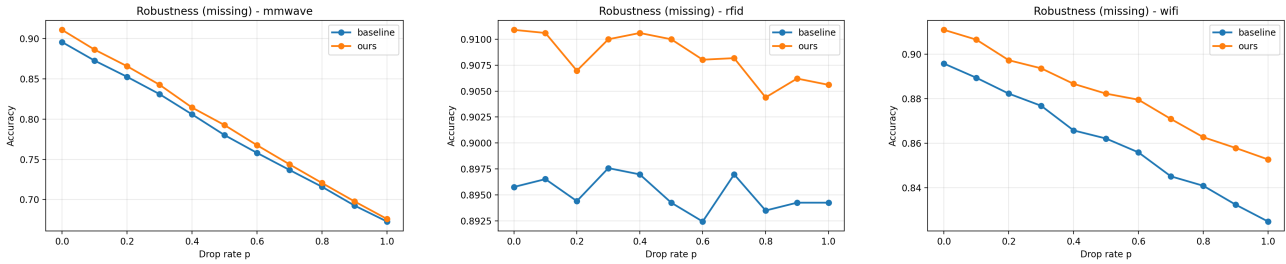


Figure 12. Robustness under random missingness on X-FI. We randomly mask temporal steps or segments of one modality with probability p at test time. From left to right: mmWave, RFID, and WiFi. DAGR maintains higher accuracy and better stability under increasing modality missingness.

Table 7. CREMA-D results with additional controls compared with contrastive/invariance-driven objectives. “Naive Align” enforces always-on per-sample cross-modal coupling. “Unit-sphere only” isolates the effect of normalization without any additional regularization losses.

Method	CREMA-D		
	Audio	Visual	Multi
Naive Align (always-on)	60.65 \pm 0.86	72.21 \pm 1.07	77.98 \pm 1.11
VICReg-style (inv+var+cov)	59.18 \pm 1.67	71.35 \pm 1.00	78.12 \pm 0.94
Barlow Twins-style (decor)	59.09 \pm 0.62	61.32 \pm 3.41	71.07 \pm 0.81
Unit-sphere only	60.65 \pm 1.30	69.84 \pm 0.22	75.81 \pm 1.52
Ours	62.98 \pm 0.50	72.10 \pm 0.55	78.16 \pm 0.38